Discrete Element Method (DEM) Contact Models Applied to Pavement Simulation

Bo Peng

Thesis submitted to the faculty of
the Virginia Polytechnic Institute and State University
in partial fulfillment of the requirements for the degree of

Master of Science
In
Civil Engineering

Linbing Wang
Montasir Abbas
Cristian Druta

June 18, 2014
Blacksburg, Virginia

Keywords: Discrete element method, contact models, pavement simulation, power-low viscoelasticity

Discrete Element Method (DEM) Contact Models Applied to Pavement Simulation

Bo Peng

ABSTRACT

Pavement is usually composed of aggregate, asphalt binder, and air voids; rigid pavement is built with hydraulic cement concrete; reinforced pavement contains steel. With these wide ranges of materials, different mechanical behaviors need to be defined in the pavement simulation. But so far, there is no research providing a comprehensive introduction and comparison between various contact models. This paper will give a detail exploration on the contact models that can be potentially used in DEM pavement simulation; in the analysis, it includes both a theoretical part, simulation results and computational time cost, which can reveal the fundamental mechanical behaviors for the models, and that can be a reference for researchers to choose a proper contact model. A new contact model–the power law viscoelastic contact model is implemented into software PFC 3D and is numerically verified. Unlike existing linear viscoelastic contact models, the approach presented in this thesis provides a detailed exploration of the contact model for thin film power-law creeping materials based on C.Y Chueng’s work. This model is aimed at simulating the thin film asphalt layer between two aggregates, which is a common structure in asphalt mixtures. Experiments with specimens containing a thin film asphalt between two aggregates are employed to validate the new contact model.

Acknowledgement

I cannot express enough thanks to my advisor for his continued support and encouragement: Dr. Linbing Wang, who sometimes is more like a friend rather than an advisor. I offer my sincere appreciation for the learning opportunities provided by him.

My completion of this research could not have been accomplished without the support of my colleagues, Wenjuan, Wenjing, Ying, Yingning, Yufeng, and my ACM's friends. Your technical advice and supports helped and inspired me.

Finally, to my caring, loving, and supportive mom and dad: my deepest gratitude. Your encouragement when the times got rough are much appreciated and duly noted. Also, it was a great comfort and relief to know that you are going to pay my bill when I run out of money. My heartfelt thanks.

Table of Contents

List of Figures and Tables

Chapter 1 INTRODUCTION

1.1 Background

Particulate systems widely exist in the natural world, for example, molecular systems, gas systems, and even fluid and solid systems, all of which can be regarded as comprised of particles. Therefore, a good simulation method to help us understand the particulate system becomes very important.

There are some popular simulation methods to capture the mechanical behavior of a particulate systems, such as the finite element method (FEM), the discontinuous deformation analysis (DDA) and the discrete element method (DEM). FEM is a continuum approach to capture the stress-strain distribution, while DDA and DEM are more focused on discontinuous materials and dynamic states. Because of its realistic simulations, simplicity, high efficiency and portability, the discrete element method is the most popular numerical methods to simulate particle system.

After discrete element method (DEM) was proposed (Cundall 1979), this method started to develop rapidly worldwide. DEM can be applied in a varied range of research, including the particle fluidization of cohesionless and cohesive particle flow, confined or unconfined particle flow, particle flow in hoppers, in mixers, in drums and mills, particle packing, compaction of particles, etc. The advantage of DEM is that it can simulate heterogeneity materials through discretization. Setting different parameters to the contributing materials in the simulation helps to distinguish their interaction.

In DEM, a finite number of sphere particles are generated to simulate different materials.

There are two types of particles in the DEM, soft particles and hard particles. The exact relationship between deformation and contact force is calculated between the soft particles. Soft particles are applied in the models such as particle packing, hopper flow, and heaping transport property models where deformation is relatively small in comparison with the overall model size, and the overall results are sensitive to the contact models. Hard particles are mostly used in large deformation simulations, such as rapid granular flow. The deformation and contact force interaction is not precisely estimated during the modeling for hard particles. So far, the soft particles are more widely used than hard particles. Given the proper initial condition and well estimated parameters in the contact models, soft particles in DEM can provide reasonable mechanical behaviors of different materials.

1.2 Research objectives

Three major objectives identified in this thesis are:

1. A review of different existing contact models shall be introduced. Three types of contact models will be presented in detail: viscoelastic model, plastic model and elastic model.
2. A power law viscoelastic normal contact model, based on the theoretical work by D. Cebon and C.Y. Cheung (1997), shall be developed. Numerical implementation of this model shall be written into a DLL file, which can be loaded in DEM software PFC 3D.
3. An X-ray microscopy experiment shall be developed to validate the numerical results of the power law viscoelastic contact models.

The ultimate objective of this research is to explore the macromechanical behavior of different contact models in DEM. In this thesis, one new power law viscoelastic contact model is developed, and six other widely used DEM contact models are reviewed.

For the new power law contact model, a power-law viscoelastic contact model with improved accuracy is developed for future simulations. So far, linear viscosity is widely used because of its simplicity, for example, the Burger model; however in a more realistic situations, creep behavior is more complex and closer to a high order equation. Cheung's theoretical solution on thin film power-law creep has been validated with experimental results (D. Cebon and C.Y. Cheung 1997); it would have a significant impact to put this solution into practice – develop a DEM contact model to be applied to asphalt binder.

For existing contact models, providing a comprehensive picture is important for assisting researchers in selecting a suitable model for specific situations. In the past there are researchers who made comparisons between different contact models; Adam and Nosonovksy(2002) compared how geometrical and material properties affect contact models; A. Renzo and Maio (2004) applied different elastic contact models in granular flow codes; Maio and Renzo (2005) modeled particle contacts by both linear and non-linear approaches. But they mainly focused on elastic contact models. A more comprehensive analysis of contact models is needed to help frame the overall picture when it comes to contact models and their application.

In this thesis, the DEM contact force-displacement relationships in normal and shear directions are presented to analyze their fundamental mechanical behavior. Practically, computational time costs for different contact models are explored, which reveals the balance between model accuracy and time cost. These six contact models can be classified into three categories including an elastic model, a ductile model and a viscoelastic model. A comparison between contact models in each type is shown in detail, providing a reference for future researchers choosing the most suitable contact model in their simulation.

1.3 Research tasks and organization

This thesis is organized into nine chapters. Chapter 1 introduces the objectives of the research. In Chapter 2, the literature review of contact models, important previous works and the principles of DEM are introduced. In Chapter 3, the methods for contact model development and verification are explained. In Chapter 4-6, the six existing contact models are described, and they are introduced separately from normal directions and tangential directions. The power law viscoelastic contact model is presented together with the experiment detail in the Chapter 7, and experimental results are compared with numerical results. Chapter 8 presents the computational costs for different contact models. Chapter 9 provides conclusions and recommendations for future work.

Chapter 2. BACKGROUND

This chapter starts with the basic principles of DEM, including the process of how particles interact with each other and how the boundary conditions are set. Then, the important research results of contact models in DEM and the parameters determination methods are reviewed.

2.1 Basic principle of DEM

2.1.1 Calculation cycle

The DEM method is a time-stepping algorithm, which means the same algorithm repeats in every time-step, and results in each time-step are based on the previous results. In the DEM system, a finite number of sphere particles interact with each other, and there are two iterations calculated in each time step:

1. Contacting forces are generated based on the overlaps between particles.
2. Movement of particles are updated based on previous movement information and current contact forces.

In the first step, the Force-Displacement law plays an important role, since the contact forces between neighbor particles are the dominant factor of resultant force changes. For each time-step, the contact forces are changed due to a Force-Displacement law in contacts.

In the second step, Newton's Second Law is the principle to evaluate how the contacting force determines the movement. Taking one particle in one time-step for example, the resultant force on a particle would be regarded as the same during this time-step; the current acceleration of the particle would be estimated by resultant force divided by mass, and the new velocity and position of this particle are obtained based on the previous position, velocity plus the integration of the current acceleration over the time-step. This is called the Law of Movement.

The above description only considers one particle; the DEM method would go through the whole the system to update their movement for each particle and the new contacting forces for all contacts for every time step.

Taking the first DEM simulation (Cundall and Strack1979) for example, in the program called BALL implementing DEM, the interaction between each sphere is guided by the following equations:

$$\mathrm{F} = \mathrm{m}\ddot{x} \tag{1}$$

$$\mathrm{F} = K_n U_n \tag{2}$$

where m is the particle mass, $\ddot{x}$ is the acceleration, F is the contact force, K_n is the stiffness for elastic material and U_n is the overlap between two particles. The first equation is the Newton's second law, and the second equation means that the contact model between particles is a linear elastic model.

In conclusion, DEM is composed of two parts: Law of motion and Force-displacement Law, as Figure 2.1 shows.

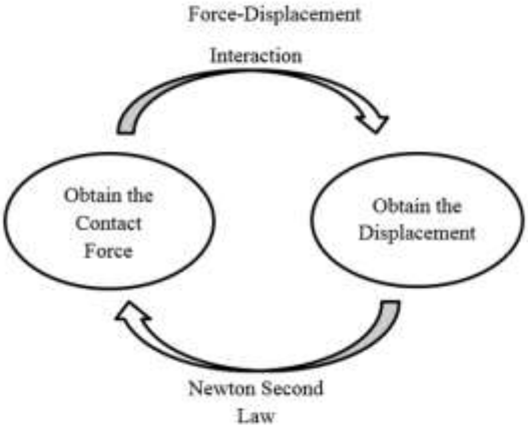

FIGURE 2.1 Flow chart of DEM principle.

2.1.2 Law of movement

The law of movement is based on the Newton Second's Law. In the particulate system, a single particle is affected by three types of forces: gravity, contact force and none-contact force, and its motion can be described as:

$$\frac{d\boldsymbol{V}}{dt}\mathrm{m}_i = \sum_j F_{ij}^{c} + \sum_j F_{ij}^{nc} + G \tag{3}$$

where V is the velocity, F_{ij}^{c} is the contact force of particle i, F_{ij}^{nc} is the non-contact force, G is the gravity.

Take the time-step into consideration, the motion of a particle is composed of five factors: its position x, velocity $\dot{x}$, acceleration $\ddot{x}$, angular velocity ω and angular acceleration $\dot{\omega}$, which are determined by the resultant force and resultant moment:

$$\ddot{\boldsymbol{x}}^{t} = \boldsymbol{F}^{\boldsymbol{t}}/\mathrm{m} \tag{4}$$

$$\dot{\boldsymbol{x}}^{t} = \ddot{\boldsymbol{x}} \times \Delta t + \dot{\boldsymbol{x}}^{\boldsymbol{t-1}} \tag{5}$$

$$\boldsymbol{x}^{\boldsymbol{t}} = \int_{t-1}^{t} \dot{\boldsymbol{x}}\, dt + \boldsymbol{x}^{\boldsymbol{t-1}} \tag{6}$$

where F^{t} is the resultant force at *t*'s time step; m is the mass of particle; $\ddot{x}^{t}$, $\dot{x}^{t}$, x^{t} is the acceleration, the velocity and the position of a particle in the *t*'s time step; $\dot{x}^{t-1}$, x^{t-1} is the velocity and displacement in *t-1* 's time step, Δt is the duration of time step. The motion of the particle in the equation is all vector based, and the direction information is included.

Besides the resultant force, the directional motion of a particle is also determined at a specific moment:

$$\mathbf{M}^{\boldsymbol{t}} = I\dot{\boldsymbol{\omega}}^{\boldsymbol{t}} \tag{7}$$

where M^{t} is the moment of time t, $\dot{\omega}^{t}$ is the angular acceleration of time t, and I is the moment of inertia of the particle. Since the shape of particles is a sphere, which means the moment of inertia is the same in all directions, and assuming the mass is evenly distributed on the sphere of radius R, the Eq. (7) can be simplified as:

$$\mathbf{M}^{\boldsymbol{t}} = I\dot{\boldsymbol{\omega}}^{\boldsymbol{t}} = (\frac{2}{5}\mathrm{m}R^2)\dot{\boldsymbol{\omega}}^{\boldsymbol{t}} \tag{8}$$

Eq. (3-8) show the basic law of motion for one particle. In the process of the one time-step, the motion calculation is executed for every particle one by one. After motion estimation is finished, the force-displacement principle will be applied to obtain the new resultant force for each particle.

2.1.3 Force-displacement principle

The force-displacement principles describe the relationship between relative movement of two particles and the contacting force.

The relative motion can be described as two independent parts: normal direction and tangential direction. The direction of normal contacting displacement is always pointing from the center of one entity to that of another, and the ‘displacement’ factor in this displacement-force principle is designated by effective overlaps. There are two types of contacts: ball-ball contact and ball-wall contact. The effective overlap in ball-ball contact is the overlap length in the line that connects two balls’ centers, as Figure 2.2 shows. For ball-wall contact, the effective overlap is equal to the radius of sphere minus the shortest distance from the center of ball to the wall, as Figure 2.2 shows.

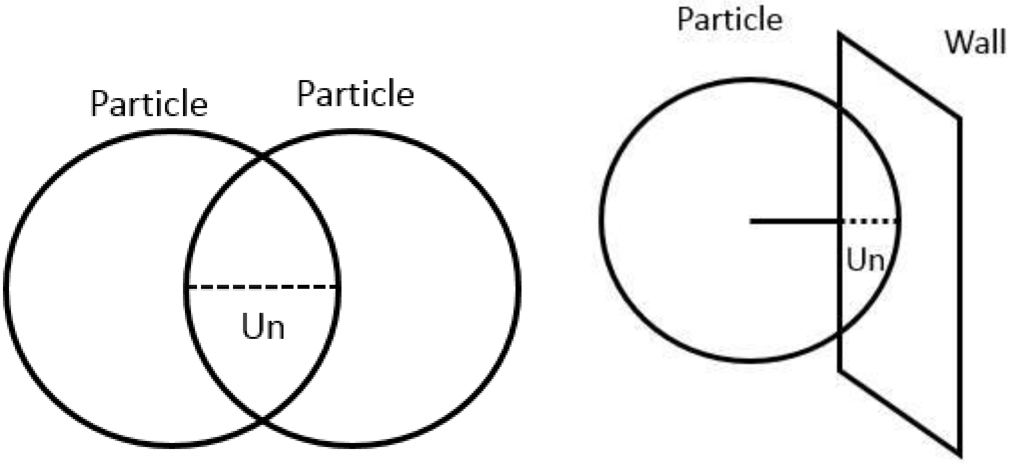

FIGURE 2.2 Ball-ball contact and ball-wall contact

The mathematic form of overlaps are:

$$u_{ij}{}^{n} = r_i + r_j - d_{ij} \tag{9}$$

$$u_{iw}{}^{n} = r_i - d_{iw} \tag{10}$$

where $u_{ij}{}^{n}$ is the overlap between entity i and j; r_i, r_j is the radius of particle i and j; d_{ij} is the distance between centers of two balls. For equation (10), $u_{iw}{}^{n}$ is the overlap between ball and wall, d_{iw} is the shortest distance between ball and wall.

For the tangential direction, the relative movement is composed of a rotation component and a translation, as Figure 2.3 shows. The mathematic form is:

$$u^{\tau} = d_{ab} + \theta \times r_i \tag{11}$$

where u^{τ} the displacement in the tangential direction, d_{ab} is the transition and θ is the rotation.

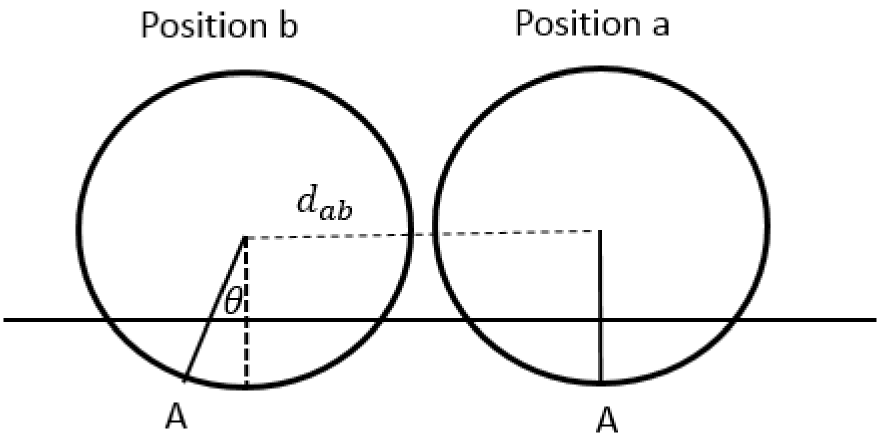

FIGURE 2.3 Definition of shear overlap

To illustrate the force-displacement relationship, Eq. (2) shows the simplest contact condition: linear elastic, but in most cases, the relationship between force and displacement is not direct enough, and normal derivatives are involved:

$$\mathrm{F} = \mathrm{g}(F, \dot{F}, \ddot{F}, U_n, \dot{U}_n, \ddot{U}_n) \tag{12}$$

To eliminate derivatives of force-displacement relationship in DEM, the finite-difference time-stepping scheme is applied to redefine the normal derivatives:

$$U = \frac{U^{t+1}+U^{t}}{2} \tag{13}$$

$$\dot{U} = \frac{U^{t+1}-U^{t}}{\Delta t} \tag{14}$$

$$\ddot{U} = \frac{\dot{U}^{t+1}-\dot{U}^{t}}{\Delta t} \tag{15}$$

$$F = \frac{F^{t+1}+F^{t}}{2} \tag{16}$$

$$\dot{F} = \frac{F^{t+1}-F^{t}}{\Delta t} \tag{17}$$

$$\ddot{F} = \frac{\dot{F}^{t+1}-\dot{F}^{t}}{\Delta t} \tag{18}$$

where U^t is the displacement in the last time step and U^{t+1} is the updated displacement at the current step. The same idea is applied to F^t and F^{t+1}. In the centered finite different time-stepping scheme, calculation stability and accuracy are not ensured unless the time step exceeds the critical time step.

2.1.4 Boundary and initial conditions

The particulate system is usually constrained by walls, which are entities without mass. Because they lack of mass, constant forces cannot be loaded in the wall. But a constant rotational velocity can be assigned for a wall. Walls have stiffness as a property, and particles are restricted on one side of the walls. Besides walls, a periodical boundary is another choice, which means a new particle would generate automatically within the boundary as soon as one particle gets out.

2.2 Contact model review

There are two major types of contact models—particle-particle and particle-fluid. The particle-particle contact is the focus in this thesis, which is the key factor for simulating different materials. Particle-particle contact models, abbreviated as contact model in the following, can be classified as contacting force models and non-contacting force models. There are four types of contact models in general: continuous potential models, elastic model, viscoelastic and plastic models, in which the first one belongs to non-contacting force model, while the other three belong to the contacting force model.

The continuous potential model is widely applied in molecular systems, which includes van der Waals forces (Hamker 1937), electrostatic forces (Krupp 1967), and liquid bridge forces. The elastic model can be sub-classified as linear elastic and nonlinear elastic models. The most widely applied linear elastic model is the simplest contact model which shows the linear relationship between overlap and contacting force as Eq. (2) describes, while the nonlinear model takes the shape of the particle into consideration; the hertz model (Hertz 1882)is the most frequently used model in non-linear elastic simulations. With the default of no energy loss taken into consideration, viscoelastic models makes up this part by adding dashpots. The frequently used viscoelastic contact model is a simple viscoelastic model, which is comprised of a spring and a dashpot, and a Burger model, which combines a Maxwell model and a Kelvin model in series. Besides simulating energy dissipation according to velocity by a dashpot, plastic model employs a spring with a different stiffness in the unloading process to simulate the energy loss.

In addition to the particle-particle contact model, DEM is able to couple with fluid. A combination of computational fluid dynamic (CFD) algorithms and DEM is applied in various fields of particle flow simulations. In this situation, particles interact with fluid—they are surrounded by fluid and their movement is resisted. There are two major methods for particle flow-fluid calculation: a continuum approach at the macroscopic scale, which is governed by balance equations and closed with initial and constitutive conditions; and a discrete approach at a microscopic level, by which motions of individual particles are analyzed without global assumptions of constitutive and uniform constituency. With different parameters and control conditions, multi-scale analysis can be employed through DEM.

Chapter 3 Methodology

3.1 Simulation

All simulations in this thesis are conducted with DEM software Particle Flow Code 3-Dimension (PFC 3D). In the part of analysis the force-displacement model, one new contact model and six existing models are included. The new contact model—the power law viscoelastic contact model—is user-defined in C++ language. After the key equation (See Eq. 78) is written into the interface between C++ and FISH, which is the official coding language for PFC 3D, a DLL file is obtained by compiling the C++ project, and this DLL file allows the new contact model to be loaded in PFC 3D directly. The other six contact models -- elastic, Hertz, simple viscoelastic, Burger, simple ductile, softening displacement – are provided by PFC 3D software itself.

In order to verify the new contact model and analyze the mechanical behavior of other contact models, a two-particle model with only one contact is developed. In verifying the power law viscoelastic model, both particles are fixed with an initial overlap, as Figure 3.1(a) shows. The computed normal contact force changing with time is recorded in the simulation, and the analytical results are compared with computed results. For the other existing contact models, normal and shear directions are analyzed separately. For the normal direction, one particle is fixed, the other moves along the direction between their centers, as shown as Figure 3.1(b). The contact overlap and contact force is recorded. To test the reaction in the shear direction, a model is developed with one completely fixed particle and the other one only center fixed. Though the center of the second particle is not able to move, a constant angular velocity is applied to it. In this way, the normal contact force stays the same while the shear contact force is observed. This is shown in Figure 3.1(c).

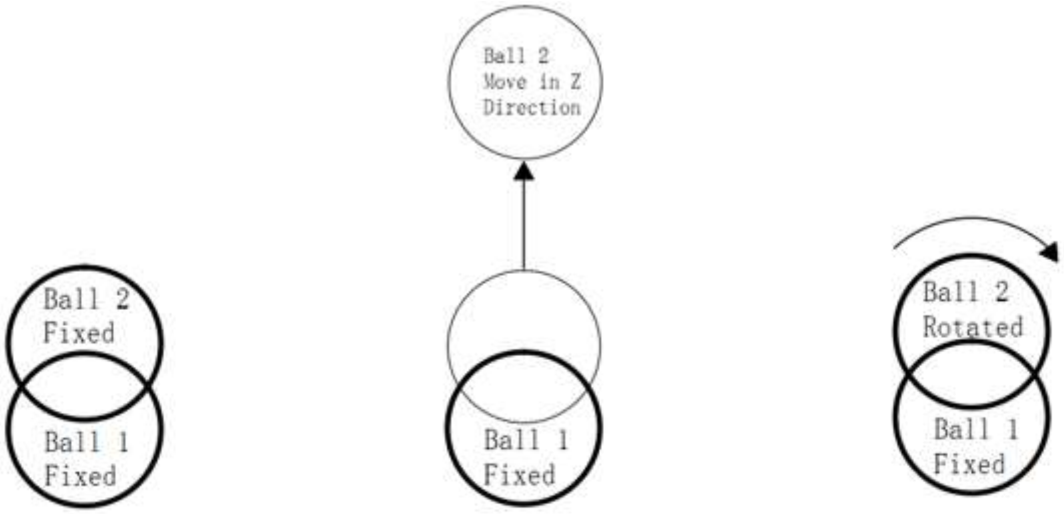

(a) Verification for new model **(b) normal directions** **(c) shear direction**

FIGURE 3.1 The model to test contact models.

In order to benchmark the computational costs for different contact models, a model of two walls sandwiching two layers of particles is developed in PDC 3D to present a thin layer of asphalt between the two rigid planes. Each layer has a shape of a square, and is composed of 10*10 particles. Two walls employ stiffness much larger than that of particles to simulate the rigidity of the wall. The six existing contact models are applied to both ball-ball contacts and ball-wall contacts. Then two walls are applied at a constant speed which the particles and the computational time for each contact models are recorded.

3.2 Experimental validation

Experimental data is used for obtaining parameters as well as comparing with DEM simulation data for validation of the new power law viscoelastic model. Considering the simulation condition only has boundaries at the top and bottom, a uniaxial compression experiment is applied.

3.2.1 X-ray tomography system

The Skyscan 1174 system, a compact micro-CT scanner as Figure 3.2 shows, is used for the experiment to validate the numerical model. With an adjustable voltage X-ray source and a range of filters for versatile adaptation, this system is able to adapt different scanning object densities. The X-ray camera is as sensitive as 1.3 megapixels, which makes scanning the whole volume of an object in a few minutes possible. In order to select different object parts for scanning easily, the system provides variable magnification from 6 to 30 µm pixel size with object positioning. Besides, the scanning system can be run by a desktop or laptop and controlled by a software, whose function includes X-ray radiography, 3D-reconstruction, 2D/3D image analysis and 3D realistic visualization. SKYSCAN provides three types of loading: tension, compression and torsion. During the loading tests tomographic scanning pictures are captured, and force-displacement data or strain-stress data is collected. In addition to scanning the surface, information about the cross-section and section perpendicular to the cross-section can also be obtained.

The loading stage of SKYSCAN is shown in Figure 3.3-3.5, which includes 5 parts. Part one (1) is a loading platform with a micro-processor which applies a constant speed, and part four is the container for samples. With an appropriate size of the specimen, it is able to achieve a uniaxial compression test with the top and bottom boundary.

FIGURE 3.2 SKYSCAN 1174 system

http://www.skyscan.be/products/1174.htm Used under fair use, 2014

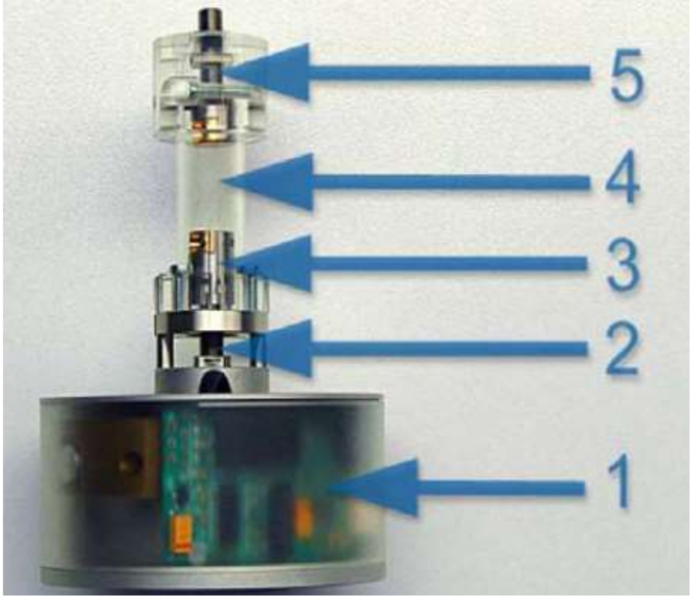

FIGURE 3.3 Testing stage of the microscopy system

http://www.skyscan.be/products/1174.htm Used under fair use, 2014

FIGURE 3.4 Sample container

Dong Wang (2007), "*Binder film thickness effect on aggregate contact behaviors*", Virginia Tech, Blacksburg, VA. Used under fair use, 2014.

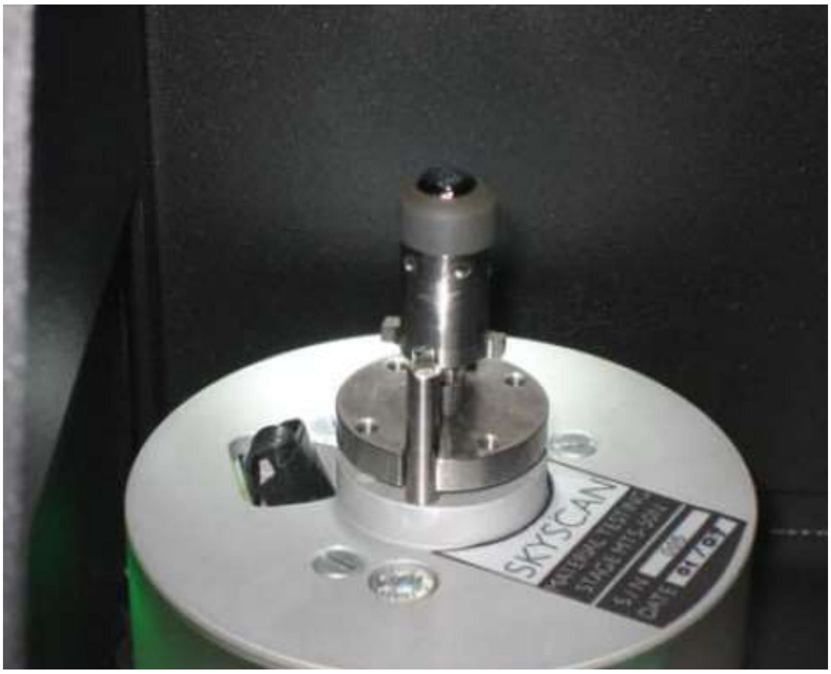

FIGURE 3.5 Loading platform

Dong Wang (2007), "*Binder film thickness effect on aggregate contact behaviors*", Virginia Tech, Blacksburg, VA. Used under fair use, 2014.

3.2.2 Sample testing

The size of a sample is mainly limited by the size of the container, part four in Figure 3.3, in SKYSCAN 1174. A layer of PG70-34 binder is placed between two squares of Unakite aggregates. The SKYSCAN is able to measure dimension information of the specimen, such as the asphalt thickness, asphalt width and aggregate size. The X-ray picture for a sample is shown as Figure 3.6.

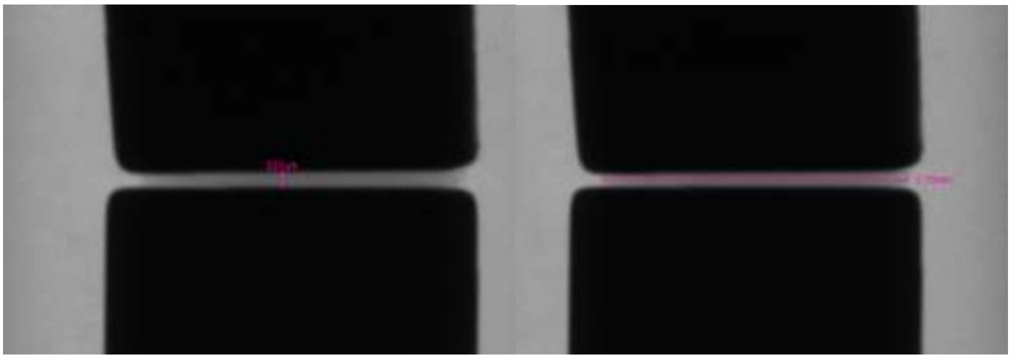

FIGURE 3.6 Test sample

After samples are placed in the loading stage, a uniaxial compression load is applied to samples from top and bottom stage. Testing parameters are set through a software to control the X-ray system. With a constant speed of 0.7 µm, the force-displacement relationship is recorded during the uniaxial compression process.

Chapter 4 ELASTIC CONTACT MODEL

4.1 Literature review

There are two types of basic models in elasticity: the linear elastic model and the nonlinear elastic model. Linear elastic models can be just simplified as a spring, while non-linear normal elastic model usually refers to hertz model, which is more complicated (Tsuji and Kawaguchi 1993; Walton et al., 1986; Walton 1993; Cundall and Strack 1979; Maw et al., 1976).

A linear elastic model was first applied in the BALL program (Cundall and Strack1979) to simulate the granular assembles in two dimensions. Even though it is the simplest contact model, Cundall believes it is able to describing the behavior of disks and spheres. Also despite its simplicity, linear elastic models show better results than more complex contact models in two-ball contact collision experiments (Renzo and Maio 2004).

Considering the shape of a sphere, the hertz model provides a non-linear solution for normal elastic contacts. For the tangential direction, a nonslip model was developed (Mindlin and Deresiewicz 1953). For the nonlinear elastic model, it can be classified into three situations (Renzo and Maio 2004): normal displacement is varying while tangential displacement is zero; normal displacement is constant while tangential displacement is varying; normal displacement and tangential displacement are varying at the same time, in which the first two conditions are commonly used in DEM to calculate force-displacement relationship. The nonlinear model is extensively used: Hertzian theory is applied to determine the stiffness for a viscoelastic model (Tsuji et al.,1992); a continuous potential discrete particle model in which a simplified Mindlin model is taken into consideration to simulate frictional force is developed (Langston et al., 1994); then a very comprehensive and more complex model based on the Hertz-Mindlin model is proposed (Thornton and Yin 1991). Later, a hertz model is incorporated with a plasticity model to determine the coefficient of restitution (Thornton 1997). The simple elastic model and the Hertz-Mindlin model are introduced in the following section, both of which are provided by PFC 3D software (PFC 3D 3.0).

4.2 Simple elastic model

A linear elastic model is the simplest and the most fundamental contact model. It shows a linear relationship between force and displacement. In the case of pavement simulation, this contact model is widely used to simulate aggregate interactions (Abbas et al., 2007). In the simple elastic model, the increment of the contact force linearly connects with the increment of the displacement in elastic model. It obeys a Hooke's law:

$$\overrightarrow{F_i^n} = K^n \overrightarrow{U^n} \tag{19}$$

where K^n is the normal stiffness, U^n is the normal overlap displacement, n_i is the unit vector whose direction is the same as the overlap displacement. The direction of normal contact force is the same as a segment connecting the two ball's center.

In the tangential direction, the shear force is a vector whose direction of change is the opposite as the increment of displacement:

$$\Delta\overrightarrow{F_i^s} = -K^s \Delta\overrightarrow{U^s} \tag{20}$$

If the two balls have different stiffness, then the contact normal secant stiffness should be a combination:

$$K^n = \frac{k_n^{[A]} k_n^{[B]}}{k_n^{[A]} + k_n^{[B]}} \tag{21}$$

Similarly, the shear stiffness is:

$$K^s = \frac{k_s^{[A]} k_s^{[B]}}{k_s^{[A]} + k_s^{[B]}} \tag{22}$$

As Figure 4.1(a) presents, the contact interaction confirms the linear relationship between force and displacement, but it can only be loaded with compression or a shear force; a tensile force is not suitable. Though the elastic contact model has a very simple mathematical expression for force-displacement relations, it is able to be applied in both static and dynamic situations and has a high stability. Researchers use this contact model to simulate a particle-surface collision test and a tamping test, where deformation is generally elastic and relatively small. It is an accurate enough model to simulate soil, cement, rock, and other elastic materials. Also because of its highest efficiency, it is widely used in very complex models.

The normal force always increases when overlap accumulates, while, as Figure 4.1(b) shows, in the shear direction, a limitation is set by friction:

$$F_s \leq \mu F_n \tag{23}$$

where μ is the friction coefficient. The limitation of shear strength is the basis of collision simulation. Different friction coefficients would influence the maximum tangential displacement, which is a critical factor in simulation.

4.3 Hertz-Mindlin Contact Model:

When the shape of the sphere is taken into consideration, a linear elastic model may not be accurate enough. In this case, the Hertz theory is developed to solve the contact mechanical behavior for sphere shapes. But because of the high complexity of the Hertz model, a more practical approach, the Hertz-Mindlin model (Mindlin and Deresiewicz 1953), should be used to replace the original one. This model is based on hertz’s theory in the normal direction and Mindlin’s no-slip improved model in the shear direction. The combination of Hertz-Mindlin theory and its application to the DEM contact model was proposed by Di Renzo and Di Maio (Renzo and Maio 2004; 2005).

For two spheres with radius of R_i, Young's modulus E_i and Poisson ratio v_i (i=1,2), that are in compression with a force P, there is a hertzian pressure relationship of:

$$P(r) = p_0(1-(\frac{r}{a})^2)^{1/2} \tag{24}$$

where:

$$p_0 = (\frac{3P}{2\pi a^2}) \tag{25}$$

$$a = (\frac{3PR^*}{4E^*})^{1/3} \tag{26}$$

Replacing P by $\boldsymbol{F_n^E}$, the resulting elastic force is expressed as:

$$\boldsymbol{F_n^E} = -\frac{4}{3}E^*\sqrt{R^*}U_n^{0.5}\boldsymbol{U_n} \tag{27}$$

$$R^* = \frac{R_iR_j}{R_i+R_j} \tag{28}$$

$$1/_{E^*} = \frac{1-v_j^2}{E_j} + \frac{1-v_i^2}{E_i} \tag{29}$$

where E^* is the equivalent Young's Modulus, and R^* is the equivalent radius of the two contacting bodies. In the tangential direction, the force-displacement curve is related to the historic normal and shear force. In this process, a micro-sliding is present, which arises from the application of Coulomb's law of micro scale friction. When sliding grows into the whole contact areas (gross sliding), the friction behavior can be shortened to Eq. (23).

The complete theory of Hertz-Mindlin is fairly complex for applying into DEM based code. Therefore, some alternative approximations which have a lower but acceptable accuracy were adopted into DEM. The resulting formulation for Hertz-Mindlin model in the shear direction is:

$$\boldsymbol{F_t} = -\frac{2}{3}(8G^*\sqrt{R^*}U_n^{0.5})\boldsymbol{U_t} \tag{30}$$

where G^* is the equivalent shear modulus of the two contact materials. This model is originally based on Mindlin (Mindlin, and Deresiewicz 1953), and later it was used in the DEM simulation and improved by Di Renzo and Di Maio. However, the Mindlin model shows poor simulation results in the case of single impact tests in the shear direction, which is even worse than the linear elastic model. Low accuracy results of using the Hertz-Mindlin model simulating both small and large impact angles is shown; either the shear force and displacement results is improperly estimated (Renzo and Maio 2005).

The relationship between force and displacement in the Hertz-Mindlin contact model is shown in Figure 4.1(c) and Figure 4.1(d). In the figure, it is clear that tensile force is not available in the Hertz-Mindlin model and the contact force increased with the increment of contact overlap. It can be also observed that the slope for the force-displacement relationship keeps increasing steadily, which is reasonable for a contact area’s increment. When two sphere centers overlap, the normal force reaches a peak.

In general, linear elastic contact model is a simple, effective contact model with relative high efficiency, and it is a more widely used model than the Hertz-Mindlin model. That is because in most of simulations the elastic property is the main factor that should be considered. But in the cases of simulation when the exact spherical shape is considered, a Hertz-Mindlin approach would be a better choice.

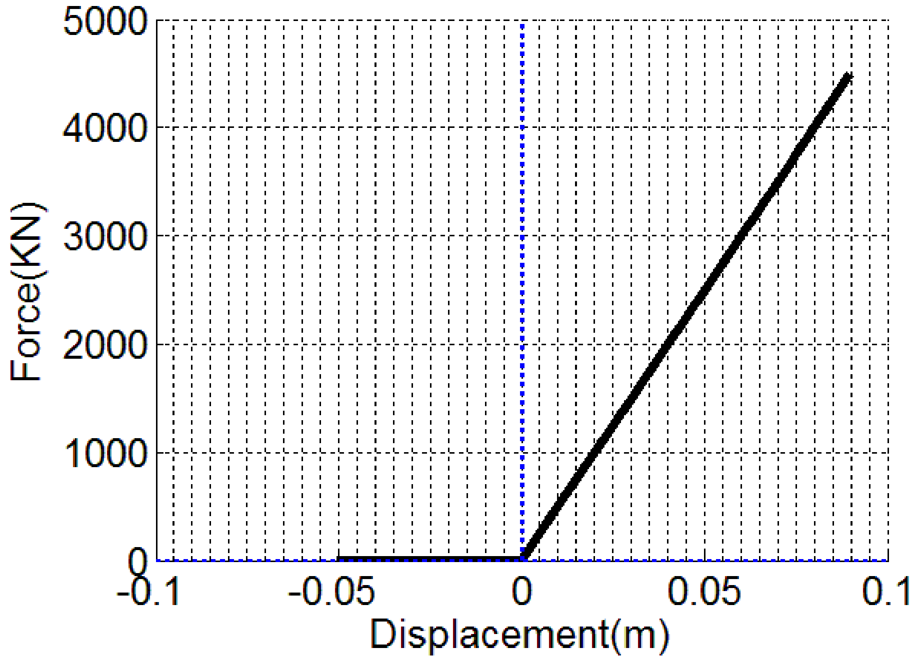

(a) Normal force-displacement curve for elastic contact model.

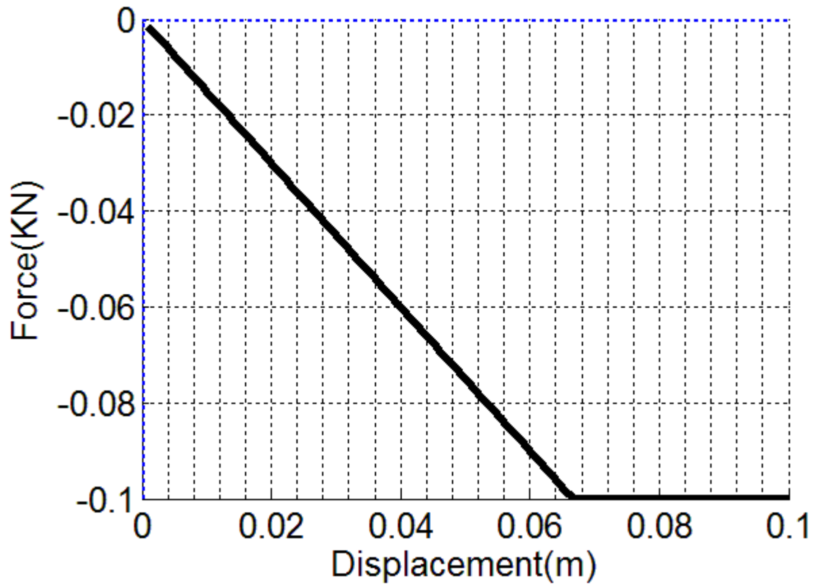

(b) Shear force-displacement curve for elastic contact model.

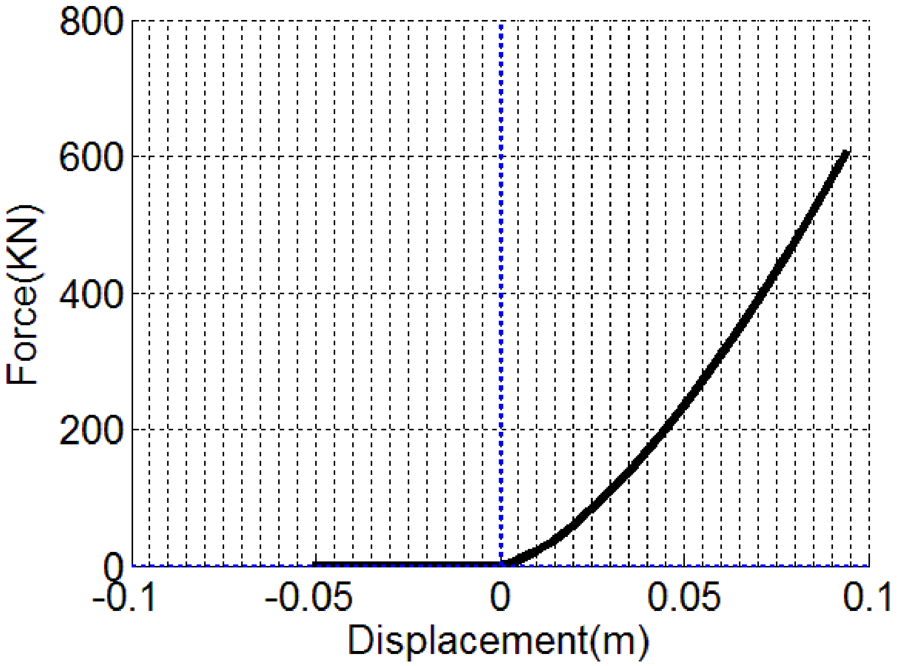

(c) Normal force-displacement curve for hertz contact model.

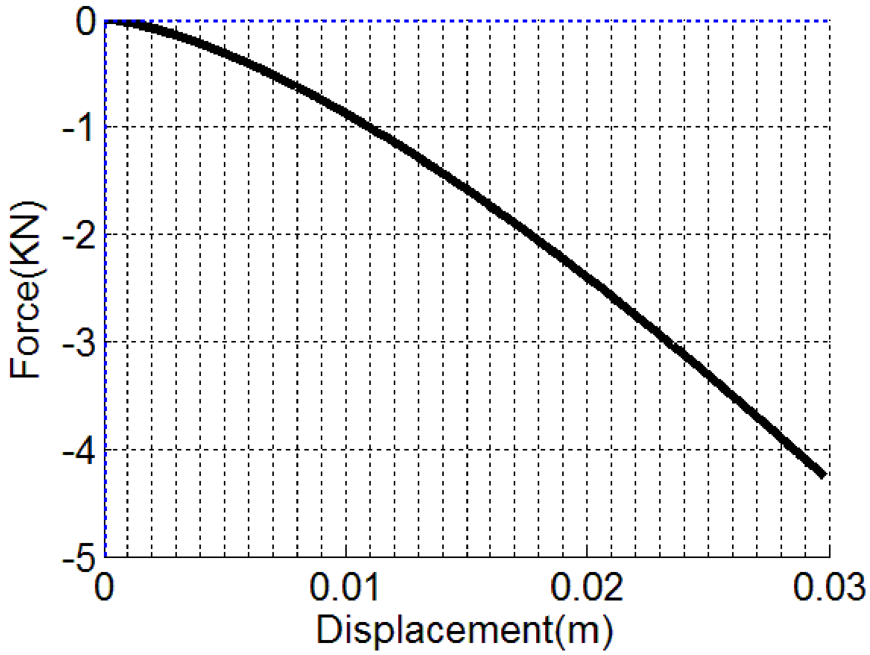

(d) Shear force-displacement curve for hertz contact model.

FIGURE 4.1 Elastic contact model analysis.

Chapter 5 PLASTIC CONTACT MODEL

5.1 literature review

An elastic model is a very ideal model that does not take energy loss into consideration. In order to simulate the energy dissipation and present the plastic deformation of the material, plastic contact models have been proposed (Vu-Quoc and Zhang 1999).

The basic idea about a plastic model is that the stiffness varies in the stage of loading, unloading and reloading. Some of these models will also change the strength of contact during the loading process.

Walton and Braun (1986) proposed a linearly model as following, which defines the stiffness in the process of loading $\dot{u} > 0$ and unloading $\dot{u} < 0$:

$$F_n = \begin{cases} -K_{n1} * u\,, & \dot{u} > 0 \\ -K_{n2} * (u - u_0), & \dot{u} < 0 \end{cases} \tag{31}$$

where K_{n1}, K_{n2} is the stiffness during loading and unloading, and u_0 is the final displacement. Sadd et al. (1993) introduced a nonlinear spring to simulate three stage loading, unloading, and reloading:

$$F_n = \begin{cases} F_{nL=} - K_{n1} * u^p\,, & \dot{u} > 0\ Loaing \\ F_{nU=} - K_{n2} * (u - u_0)^{p+q}, & \dot{u} < 0\ Unloading \\ F_{nrL=}(\varphi F_{nL} + (1 - \varphi) F_{nU}), & \dot{u} > 0\ Reloading \end{cases} \tag{32}$$

where p, q are exponents for nonlinear force-displacement law in the loading and unloading process separately. In the following section, the simple ductile model and the displacement softening models provided by PFC 3D are analyzed, highlighting methods where strength changes during the loading process.

5.2 Simple ductile contact model

Ductility is the ability for a solid material to deform under a tensile stress, and it is a common property in metal materials, and a ductile damage in metals is the essential damage that is caused by growth of cavities due to large deformations (Baumgaertel and Winter 1989). In the reinforced pavement, steel is widely used to enhance the pavement’s tensile strength. Since ductility is a form of plasticity, an understanding of plastic materials is the basis of a ductile simulation.

A theory for elastic-ideal plastic behavior of spheres was defined by Thornton (1998). This theory is then developed into a model that is applied in DEM by Tomas (2003). In his model, a hertz elastic contact approach is applied in DEM. But because of its complexity, a more widely used plastic-ductile model which involves a linear elastic behavior is introduced below.

According to continuum damage mechanics, the deterioration of a material changes at different stages of loading. A damage variable shows the change of element surface area S to $\widetilde{\mathrm{S}}$ due to the loading (Chow and Wang1987):

$$\mathrm{D} = \frac{S - \widetilde{\mathrm{S}}}{S} \tag{33}$$

With the effective surface for shrinkage, the Cauchy stress changes with the effective resisting area (Chow and Wang1987):

$$\widetilde{\sigma} = \sigma\frac{\widetilde{\mathrm{S}}}{S} = \frac{\sigma}{1-D} \tag{34}$$

Similarly, in the contact model, the normal strength f_{max}^{n} would decrease with the effective resisting area after contact reaches the tensile strength F_{t}^{n}. In a simulation, the change in effective areas simplifies as linear with plastic deformations U_p as the simulation result shows in Figure 5.1:

$$\mathrm{f}_{max}^{n} = \frac{\tilde{\mathrm{S}}}{S}\mathrm{F}_{t}^{n} = \frac{U_{pmax} - U_{p}}{U_{pmax}}\mathrm{F}_{t}^{n} \tag{35}$$

In the case of compression loadings, shear loadings before a model slip and tension loading before a model necking, the contact model obeys Hooke's law as Figure 5.1 shows.

The shear strength is related with the tensile strength when a tensile force is applied: $\mathrm{f}_{max}^{n} = \alpha\mathrm{F}_{t}^{n}$, where α is a coefficient; the shear strength is related to friction after the contact bond is broken in compression $\mathrm{f}_{max}^{n} = \mu \mathrm{f}^{n}$, where μ is the friction coefficient.

Figure 5.1(a) shows that the contact only yields in tension, while the contact force is linear with displacement in compression. Before the contact yields, the unloading curve is the same as the loading curve. After yielding, the unloading curve is a straight line point directly to the (0,0) point, which means, there is no plastic deformation existing even after yielding; this is the weakness of the simple ductile model.

Figure 5.1(b) is the force-displacement curve in the shear direction. It is linear elastic in the shear direction. The shear strength limitation only exists in tension, and there are no shear strength limitations in compression.

5.3 Displacement softening model

Plasticity is a very important mechanical behavior for steel and a displacement softening model is a good tool to simulate plasticity. Compared to a simple ductile contact model, a displacement softening model provides more details on the material plastic behavior.

In tension, the contact strength is regarded as a linear function with angle α, which is the angle between the contact force and the line segment connecting the center of two balls:

$$F_{max} = (1 - \frac{2\alpha}{\pi})F_{c}^{n} + \frac{2\alpha}{\pi}F_{c}^{s} \tag{36}$$

Yielding only happens in tension after the contact force is larger than the contact strength:

$$\mathrm{F} = \sqrt{F^{n2} + F^{s2}} > F_{max} \tag{37}$$

After the material yields, the increment of the displacement $\triangle U^k (k = n, s)$ is composed of two parts:

$$\triangle U^k = \triangle U_e^k + \triangle U_p^k \tag{38}$$

In order to obtain the plastic displacement, a 'flow rule' is applied:

$$\triangle {U_p}^k = \triangle \lambda \frac{F^k}{F} \tag{39}$$

The corresponding increment of force is:

$$\triangle F^k = K^k \triangle U_e^k \tag{40}$$

In compression, the shear contact strength is composed of friction and shear strength:

$$F_{max}^s = \mu |F^n| + F_c^s \tag{41}$$

The contact strength decreases with the increment of plastic strength:

$$\mathrm{F}_c^k (U_p / U_{pmax}) = F_c^k (1 - \frac{U_p}{U_{pmax}}) \tag{42}$$

Figure 5.1(c) and (d) present the force-displacement curve for the softening displacement model. In the normal direction, strength decreases after the contact yields. If the model unloads before contact yields, the contact force goes back along the same line of loading, which is same as a simple ductile model. But after yielding, the unloading line retreats only with the same slope of the loading line, which means plastic deformation occurred. This makes the model closer to the reality in comparison with a simple ductile model. Figure 5.1(d) shows that the model would also yield in the shear direction, and this behavior is not shown in simple ductile model.

From the Figure 5.1 (e), it is clear that if the contact is loading a tensile force in the normal direction, then the total strength that combines both shear and normal direction has a limitation, and the plastic deformation shares the same direction of the resultant force. On the other hand, in the case of compression in the normal direction, contact strength always increases when compression force is increasing, and the plastic deformation only occurs in the shear direction.

In conclusion, though both the softening displacement model and the simple ductile model is able to present ductility in the normal direction, the simple ductile model fails to take yielding behavior in the shear direction into consideration, nor the direction of plastic deformation according to compression force, all of which are important factors for the contact model closer to the real metal material behavior. But all these details and higher accuracy are based on the sacrifice of more computational costs, which is also an important consideration in large model simulations.

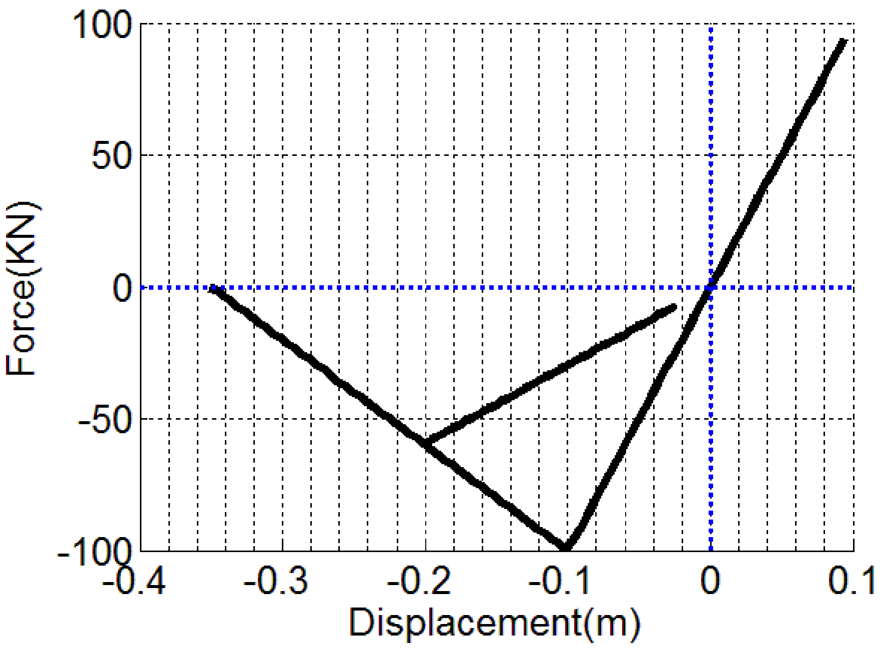

(a) Force-displacement curve for simple ductile model in normal direction.

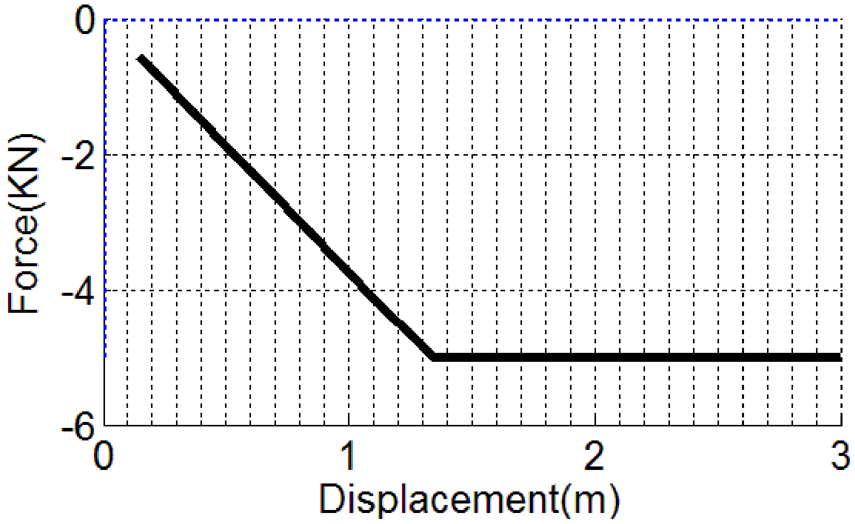

(b) Force-displacement curve for simple ductile model in shear direction.

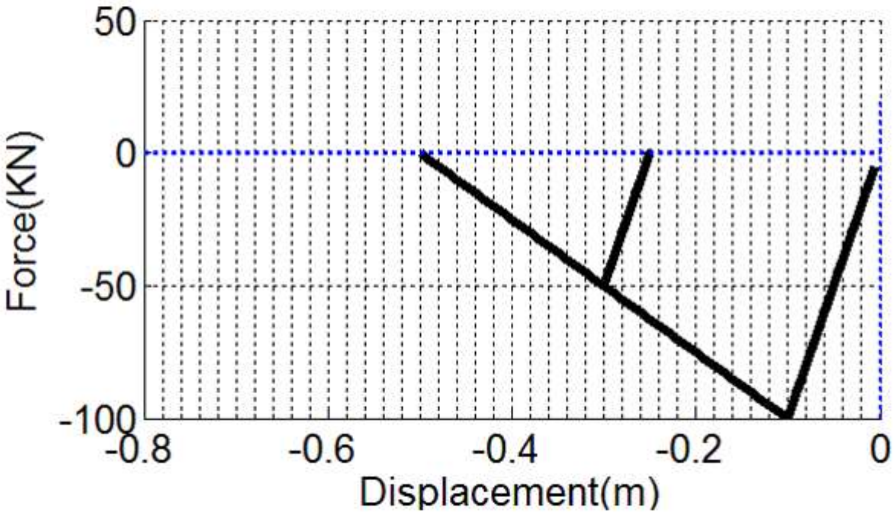

(c) Normal force-displacement curve for displacement softening model

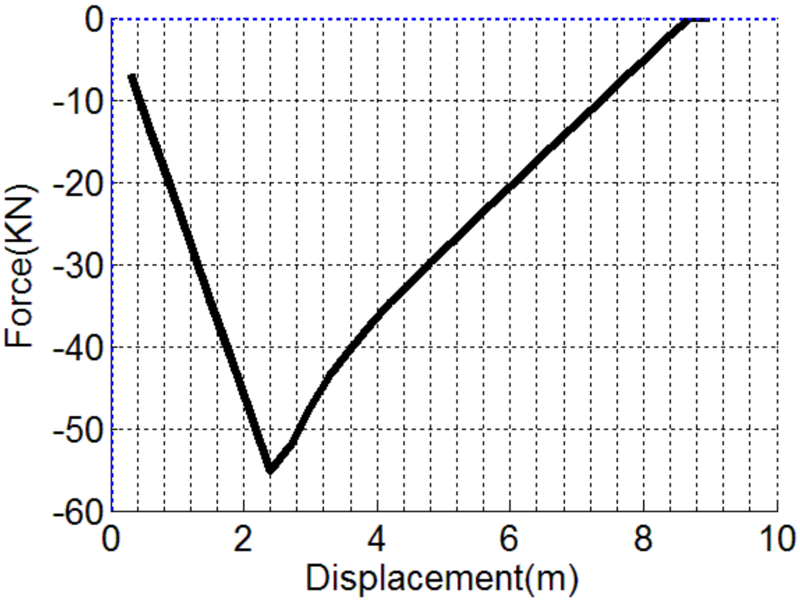

(d) Shear force-displacement curve for displacement softening model

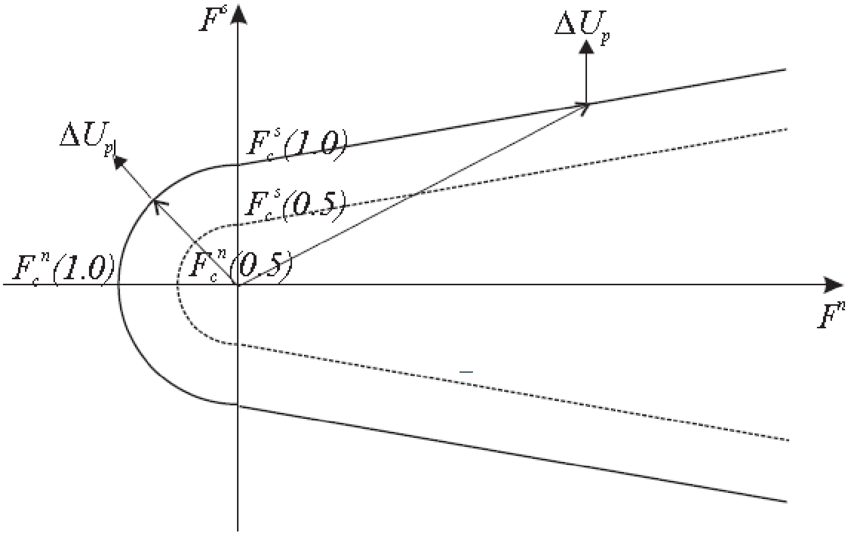

(e) Contact strength in shear and normal direction for displacement softening model

Itasca. *Particle flow code 3D manual: Background and theory*. Minneapolis, Minnesota, 2008. Used under fair use, 2014.

FIGURE 5.1 Ductile contact model analysis

Chapter 6 VISCOUSELASTIC CONTACT MODEL

6.1 literature review

A viscoelastic model is comprised of an elastic part and a energy dissipation part, which is presented by a spring and a dashpot in DEM; there are two types of combinations—a Kelvin model, which connects a spring and a dashpot in parallel, and the Maxwell model, which connects a spring and a dashpot in series. Different combinations of Maxwell model and Kelvin model can be assembled to simulate varied viscoelastic contact models.

Regarding the equation of viscoelastic models, Kruggel-Emben et al. (2007, 2008) categorized it into linear and nonlinear types. The Linear viscoelastic model in the normal direction can be simply written as:

$$\boldsymbol{F_n} = \boldsymbol{F_n^{el}} + \boldsymbol{F_n^{diss}} = -K_n\boldsymbol{u} - \eta\dot{\boldsymbol{u}}_{\boldsymbol{n}} \tag{43}$$

where K_n is the normal stiffness of the spring and η is the normal viscosity of damper. Schafer (1996) provided a detailed analysis, and obtained the velocity independent coefficient of restitution for this model.

For nonlinear viscoelastic models, a hertz model is widely used for the elastic part. For example, Lee and Herrmann (1993) proposed the following model:

$$\boldsymbol{F_n} = \boldsymbol{F_n^{el}} + \boldsymbol{F_n^{diss}} = -\widetilde{K_n}\boldsymbol{u}^{3/2} - m^{eff}\eta\dot{\boldsymbol{u}}_{\boldsymbol{n}} \tag{44}$$

where,

$$\widetilde{K_n} = -\frac{4}{3}E^*\sqrt{R^*} \tag{45}$$

where m^{eff} is the effective mass: $m^{eff} = m_i m_j/(m_i + m_j)$,and E^* and R^* can be obtained by Eq. (28) and Eq.(29). This is a partly non-linear viscoelastic contact model because the energy dissipation part is still linearly depended on velocity.

A fully nonlinear model is developed by Kuwabara and Kono (1987):

$$\boldsymbol{F_n} = \boldsymbol{F_n^{el}} + \boldsymbol{F_n^{diss}} = -\widetilde{K_n}\boldsymbol{u}^{3/2} - m^{eff}\eta\dot{\boldsymbol{u}}_{\boldsymbol{n}}\boldsymbol{u}^{1/2} \tag{46}$$

Tsuji(1992) also proposed a Hertz based model, where a slight change is applied in the viscosity part:

$$\boldsymbol{F_n} = \boldsymbol{F_n^{el}} + \boldsymbol{F_n^{diss}} = -\widetilde{K_n}\boldsymbol{u}^{3/2} - m^{eff}\eta\dot{\boldsymbol{u}}_{\boldsymbol{n}}\boldsymbol{u}^{1/4} \tag{47}$$

whose constant coefficient of restitution is constant. Kruggel-Emben et al. (2007) proposed an extended nonlinear contact model, whose stiffness and viscosity constant is limited by boundary conditions according to experiment results.

Viscoelastic models are frequently used in simulations of asphalt and liquid material. Kruggel-Eden et al.(2007) applied it to simulate granular flow; Limtrakul et al. (2004) modeled a gas-solid fluidized bed. Papagiannakis et al. (2002), Abbas et al. (2007), Shalaby(2002) simulated asphalt binders with it. The following contact models provided by PFC 3D-- simple viscous model and Burger model are introduced, both of which are linear models.

6.2 Simple viscous model:

The most important mechanical property for asphalt is viscosity; a simple viscous contact model is composed of a spring and a dashpot in the shear direction and a spring in normal direction, which is shown in Figure 6.1. In the model, the total shear velocity can be decomposed into an elastic and a viscous part:

$$\dot{u}_s = \dot{u}_s^e + \dot{u}_s^v \tag{48}$$

where:

$$\dot{u}_s^e = \frac{F_s^{t+1}{}' - F_s^{t}{}'}{k_s \Delta t} \tag{49}$$

$$\dot{u}_s^v = \frac{F_s^{t+1}{}' + F_s^{t}{}'}{2\eta} \tag{50}$$

where k_s is the shear stiffness, η is the viscosity. This is the most commonly used method. Zhang (1996) has explored the damping and spring model for viscoelasticity. In his paper, the spring in the simple viscous model can be replaced with a non-linear Hertz model, and it shows that the equation of motion with either linear or non-linear terms is reasonable.

The force-displacement curve for a simple viscoelastic contact model is shown in Figure 6.2 (a-b). It can be seen that linear the elastic behavior is shown in the normal direction, including both tension and compression, while viscosity only exists in the shear direction. This suggests that the simple viscoelastic model might overestimate the strength in a simulation, because it neglects viscosity in the normal directions.

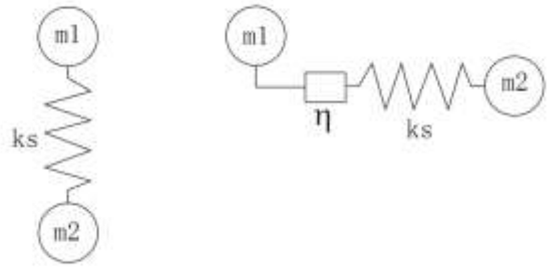

(a) Simple viscoelastic contact model

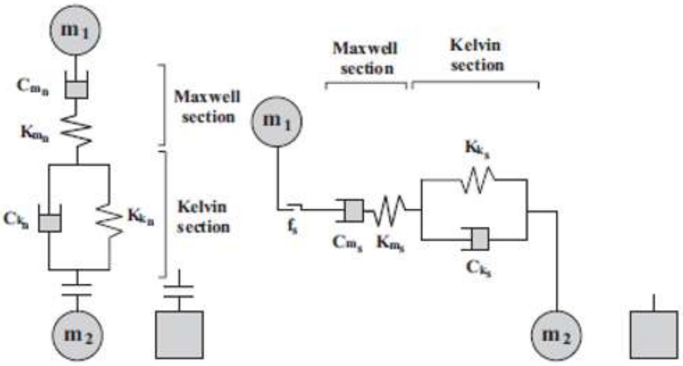

(b) Burger contact model principle

Itasca. *Particle flow code 3D manual: Background and theory*. Minneapolis, Minnesota, 2008. Used under fair use, 2014.

FIGURE 6.1 Structure for viscoelastic model.

6.3 Burger Model

The Burger model is a very popular model to simulate the creep behavior. It contains two parts: one is a Kelvin model and another is a Maxwell model. Compared to a simple viscoelastic model, results of a Burger model are closer to the real world, and the combination of Kelvin and Maxwell models improve accuracy over a simple viscoelastic model. The structure of the Burger model is shown in Figure 6.1(b).

The total displacement of the model:

$$\mathrm{u} = u_k + u_{mk} + u_{mc} \tag{51}$$

where u_k is the displacement in Kelvin model, u_{mk}, u_{mc} are the elastic part and viscosity displacement of the Maxwell model. Using the Kelvin model, the contact force is given by:

$$\mathrm{f} = K_k u_k + C_k \dot{u}_k \tag{52}$$

Using a Maxwell model, the contact force is:

$$\mathrm{f} = K_m u_{mk} \tag{53}$$

$$\mathrm{f} = C_m u_{mc} \tag{54}$$

Take the first and second derivative of the Eq.51 and combining Eqs. (52-54):

$$\mathrm{f}+\left[\frac{c}{K_k}+C_m\left(\frac{1}{K_k}+\frac{1}{K_m}\right)\right]\dot{\mathrm{f}}+\frac{C_kC_m}{K_kK_m}\ddot{f}=C_m\dot{u}+\frac{C_kC_m}{K_k}\ddot{u} \tag{55}$$

where C_k,C_m are the viscosity for Kelvin and Maxwell models, and K_k K_m are the stiffness of Kelvin and Maxwell models correspondingly. This second order normal differential equation time is the key equation to simulate the mechanical behavior of asphalt. Though the force-displacement relationship has been achieved, it is still not enough, because the derivative of this equation cannot be solved in the DEM based code directly. Using the finite-difference time-stepping scheme (Eq. 13-18) to rewrite it, a final force-displacement equation can be directly applied in DEM to obtain:

$$F^{t+1}=\frac{1}{\frac{\Delta t}{2C_kA}+\frac{1}{K_m}+\frac{\Delta t}{2C_m}}\left[u^{t+1}-u^t\right]+\left(1-\frac{1-\frac{K_k\Delta t}{2C_k}}{1+\frac{K_k\Delta t}{2C_k}}\right)u_k^t-\left(\frac{\Delta t}{2C_kA}-\frac{1}{K_m}+\frac{\Delta t}{2C_m}\right)f^t \tag{56}$$

From this equation, the contact force is able to be updated in each time step through contact force and displacement in the previous time step f^t, u^t.

These parameters in the Burger model can be determined by the methodology developed by Baumgaertel and Winter (1989). This method tests a mastics specimen and fits the Burger model to DSR measurements; specifically, the fitting procedure minimizes an objective function. However, according to Abbas (2007) this procedure might underestimate the parameters, since comparing the stiffness of asphalt to aggregate is too low, which affects the results.

Generally speaking, the Burger model is able to simulate the viscoelastic behavior accurately. To verify this, a model of two fixed balls with an overlap is built, as Figure 3.1(a) shows. Results show in Figure 6.1 (c), which presents the compression force decreasing to zero with time.

Figure 6.1 (d) presents the contact force-displacement curve in the normal direction, in which it shows that Burger model only has viscosity under compression. Force in the contact decreases to zero before the contact overlap reaches zero. This attributes to creep occurring during the particles' separation movement. The compression force keeps decreasing to be a negative number before overlap decrease to zero. After overlap equals to zero, the contact force stops changing and finally the contact breaks when overlap reaches a certain value. In the shear direction, Figure 6.1(e) shows that contact force increases first and then decreases after a peak is reached while the shear displacement steadily increased; this trend resulting from the combination of Maxwell and Kelvin models.

In comparison between simple viscoelastic and Burger models, one may conclude that the Burger model is a better choice for simulating a compression loading, for the reason that the simple viscoelastic model only presents linear elasticity in normal direction. In addition, due to the combination of Maxwell and Kelvin models, the Burger model more accurately simulates viscosity.

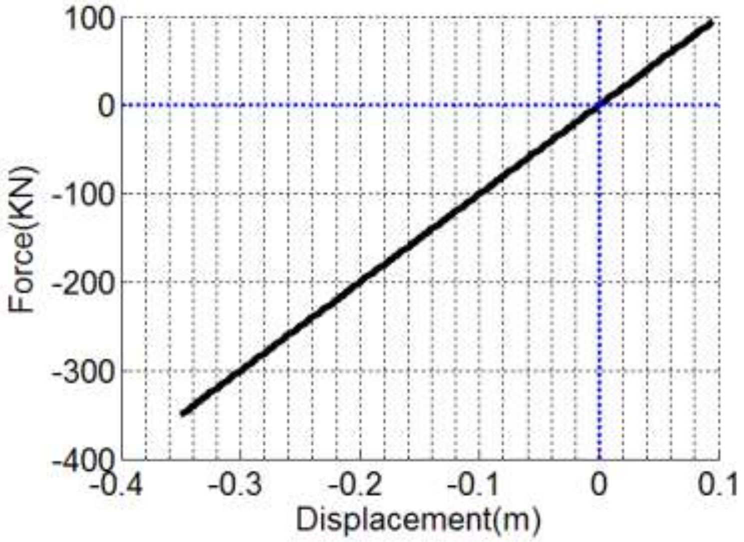

(a) Normal force -displacement curve for simple viscous contact model.

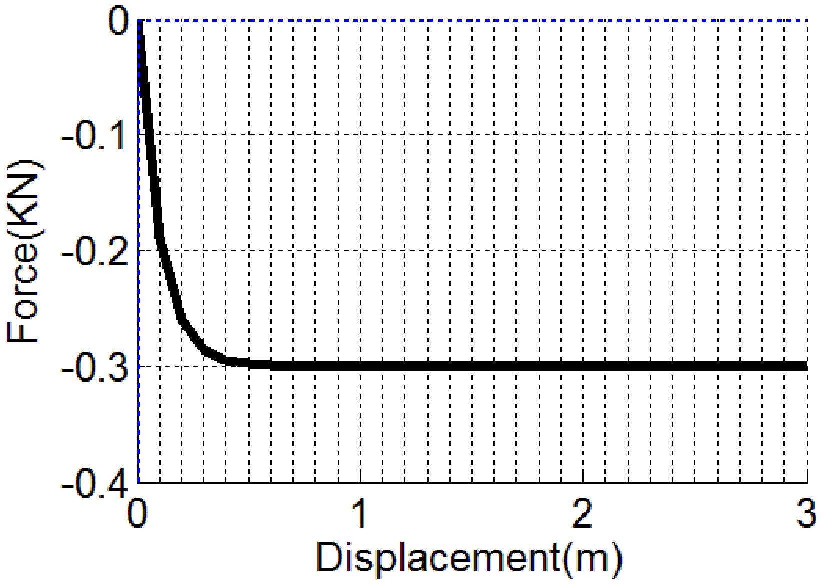

(b)Shear force-displacement curve in compression for simple viscous contact model.

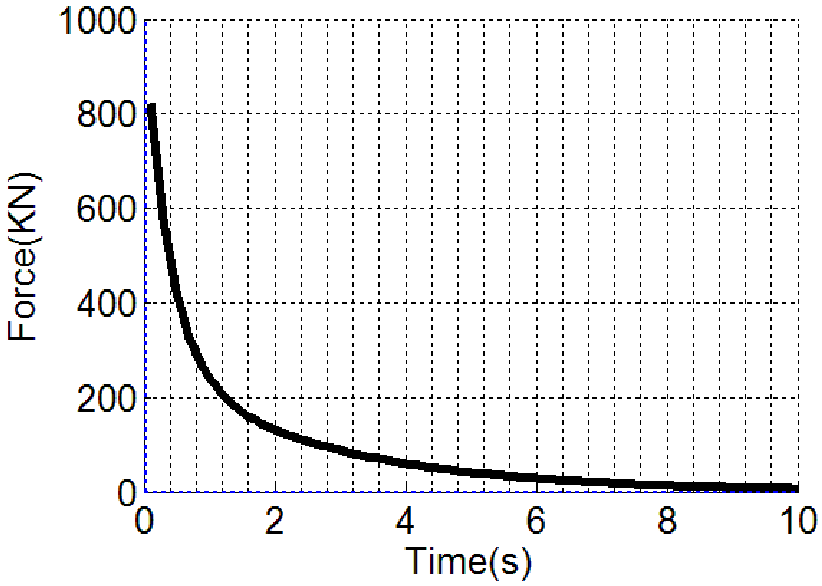

(c) Time vs force curve for two fixed ball with burger contact model.

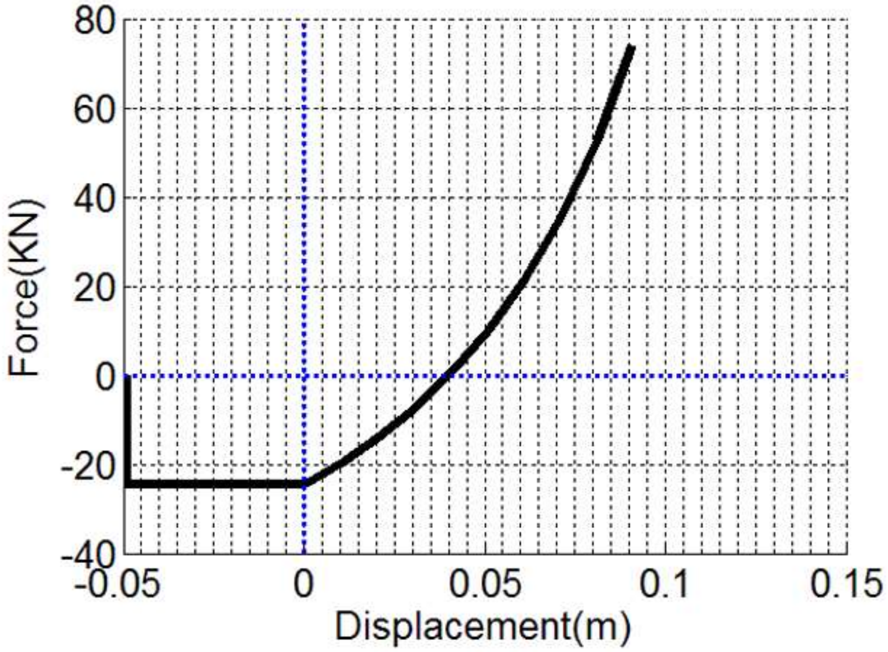

(d) Normal force-displacement curve for simple burger contact model.

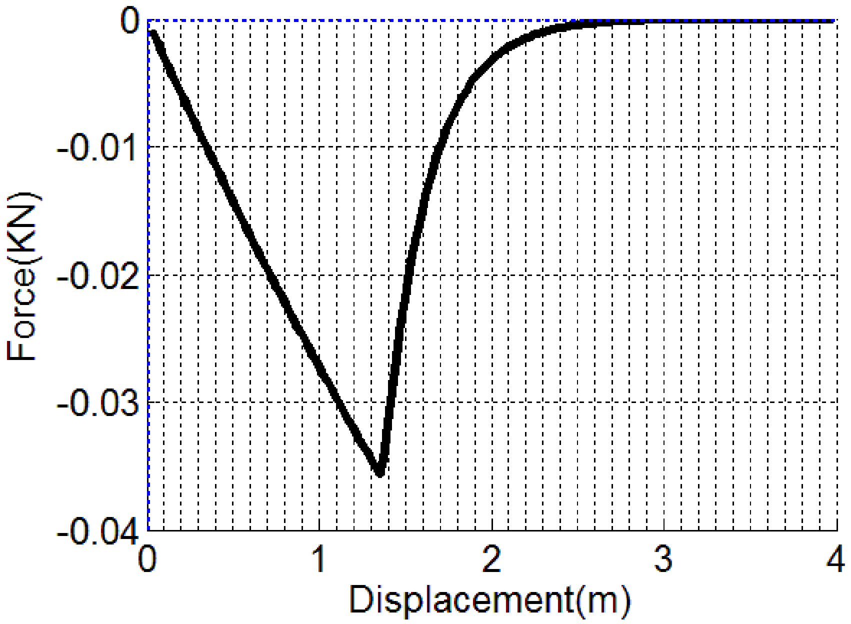

(e) Shear force-displacement curve for simple burger contact model.

FIGURE 6.2 Viscoelastic contact model analysis.

Chapter 7 POWER LAW VISCOELASTIC CONTACT MODEL

This is part is published as a proceeding paper in the conference “International Association of Asphalt Pavement” in 2014 with co-author Dr. Linbing Wang.

7.1 Theoretical deduction

Asphalt binder is usually considered as a viscous fluid at relatively high temperatures, and an elastic medium at relatively low temperatures. In the temperature range of pavement, asphalt is regarded as a viscoelastic material. A viscoelastic model is usually comprised of an elastic part and an energy dissipation part, which is presented by a spring and a dashpot. There are two types of common combinations—the Kelvin model which connects a spring and a dashpot in parallel and the Maxwell model which connects spring and dashpots in series. Different combinations of the Maxwell and Kelvin models can be assembled to come up with various viscoelastic models.

To simulate the complexity of a real viscous material, a nonlinear Maxwell model that theoretically assumes unidirectional flow in a uniform passage was developed by C.Y. Chueng and D. Cebon (1997). This solution is aimed at acquiring the relationship between force and displacement of a thin-film asphalt layer sandwiched between two aggregates. Simplifying the two aggregate surfaces as two parallel rigid planes, the specimen employed is shown in Figure 7.1. Chueng verified his solution in compression, shear and combined compression and shear by comparison with experimental results. The following theoretical content is based on a paper of Chueng’s (1997).

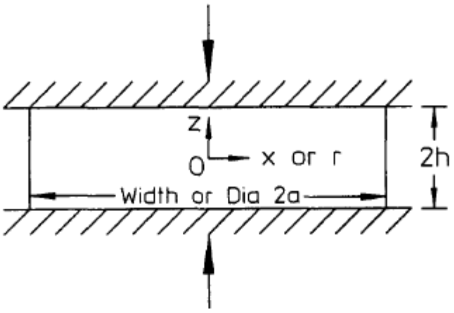

FIGURE 7.1 Geometry information of the thin layer
Cheung, C., and Cebon, D. (1997). "Thin film deformation behavior of power-law creeping materials." ***Journal of engineering mechanics*****, 123(11), 1138-1152. Used under fair use, 2014.**

This solution assumes that the width of the layer is much larger than the height of the layer. As Figure 7.1 shows, 2a is the width, 2h is the height and 2l is the length. Due to the large aspect ratio, a/h, this model can be regarded as a plane strain problem. Influenced by surrounding temperature and the characteristics of creeping material itself, pure bitumen in a thin film would follow a power-law relationship as:

$$\frac{\sigma_{ij}'}{\sigma_0} = \frac{2}{3}\left(\frac{\dot{\varepsilon}_e}{\dot{\varepsilon}_0}\right)^{1/n}\frac{\dot{\varepsilon}_{ij}}{\dot{\varepsilon}_e} \tag{57}$$

where σ_{ij} is deviatoric stress tensor; $\dot{\varepsilon}_{ij}$=strain rate sensor; $\dot{\varepsilon}_e$=effective strain rate; and $\sigma_0, \dot{\varepsilon}_0$ is a constant, which is related to the ambient temperature. If n=1, then this solution becomes linear viscosity; while in the case of n>1, the power law creep behavior is assigned to the material layer. Use the equation above, the constitutive equation can be written as:

$$\sigma_{xx} - \sigma_m = \frac{2}{3}\frac{\sigma_0}{\dot{\varepsilon}_0^{1/n}}(\dot{\varepsilon}_e)^{(1-n)/n}\left(\frac{\partial\dot{u}}{\partial x}\right) \tag{58}$$

$$\sigma_{zz} - \sigma_m = \frac{2}{3}\frac{\sigma_0}{\dot{\varepsilon}_0^{1/n}}(\dot{\varepsilon}_e)^{(1-n)/n}\left(\frac{\partial\dot{w}}{\partial z}\right) \tag{59}$$

$$\tau_{xz} = \frac{1}{3}\frac{\sigma_0}{\dot{\varepsilon}_0^{\frac{1}{n}}}(\dot{\varepsilon}_e)^{\frac{1-n}{n}}\left(\frac{\partial\dot{u}}{\partial z} + \frac{\partial\dot{w}}{\partial x}\right) \tag{60}$$

where σ_m is the mean stress. Besides the constitutive condition, the equilibrium conditions are:

$$\frac{\partial \sigma_{xx}}{\partial x} + \frac{\partial \tau_{xz}}{\partial z} = 0 \tag{61}$$

$$\frac{\partial \sigma_{zz}}{\partial z} + \frac{\partial \tau_{xz}}{\partial x} = 0 \tag{62}$$

Then, let's take a look at the strain rate sensor for this situation:

$$\dot{\varepsilon}_{ij} = \begin{bmatrix} {\partial \dot{u}}/{\partial x} & 0 & {1}/{2}\,({\partial \dot{u}}/{\partial z} + {\partial \dot{w}}/{\partial z}) \\ 0 & 0 & 0 \\ {1}/{2}\,({\partial \dot{u}}/{\partial z} + {\partial \dot{w}}/{\partial z}) & 0 & {\partial \dot{w}}/{\partial z} \end{bmatrix} \tag{63}$$

where $\dot{u}$ is the deformation rate in *x* direction, $\dot{w}$ is the deformation rate in *z* direction.

Because of the large aspect ratios in thin film model, ${\partial \dot{u}}/{\partial z}$ in strain rate tensor would be much larger than any deformation in other directions. Therefore, the strain rate tensor can be written as:

$$\dot{\varepsilon}_{ij} = \begin{bmatrix} 0 & 0 & {1}/{2}\,({\partial \dot{u}}/{\partial z}) \\ 0 & 0 & 0 \\ {1}/{2}\,({\partial \dot{u}}/{\partial z}) & 0 & 0 \end{bmatrix} \tag{64}$$

The effective stress in the case can be simplified as:

$$\dot{\varepsilon}_e = ({\partial \dot{u}}/{\partial z})/\sqrt{3} \tag{65}$$

Simplify the constitutive equation (60) and equilibrium equation (61) by Eq. (65), we can get:

$$\frac{\tau_{xz}}{\sigma_0} = \left(\frac{1}{\sqrt{3}}\right)^{(n+1)/n} \left(\frac{|\partial \dot{u}/\partial z|}{\dot{\varepsilon}_0}\right)^{1/n} \operatorname{sign}\left(\frac{\partial \dot{u}}{\partial z}\right) \tag{66}$$

$$\frac{\partial P}{\partial x} = \frac{\partial \tau_{xz}}{\partial z} \tag{67}$$

where P=-σ_m. Because of the symmetry of structure, $\partial \tau_{xz}$= 0 when z=0 and ignorance of the changing of pressure in the direction of z, the combination of the Eqs. (66, 67) can be written as:

$$\frac{\dot{u}}{\partial z} = \left(\frac{\sqrt{3^{n+1}}\dot{\varepsilon}_0}{(n+1)\sigma_0^n}\right)^{(n+1)/n} |z|^n \left|\frac{\partial P}{\partial x}\right|^n \operatorname{sign}\left(\frac{\partial P}{\partial z}\right) \tag{68}$$

Take the boundary condition that $\dot{u} = 0$ at z=±h into consideration and integrate the Eq. (68), it turn to be:

$$\dot{u} = \left(\frac{\sqrt{3^{n+1}}\dot{\varepsilon}_0}{(n+1)\sigma_0^n}\right)^{\frac{n+1}{n}} (|z|^n - h^{n+1})|\frac{\partial P}{\partial x}|^n\text{sign}(\frac{\partial P}{\partial z}) \tag{69}$$

For the overall thin film, compression of material would lead to a flow from the center to the side. Take $\dot{Q}$ as volumetric flow in the x-direction:

$$\frac{\dot{Q}}{2l} = -2\dot{\mathrm{h}}\mathrm{x} \tag{70}$$

Then we can obtain the flow rate of x-direction as:

$$\frac{\dot{Q}}{2l} = \int_{-h}^{h} \dot{u}dz = \left(\frac{2\sqrt{3^{n+1}}\dot{\varepsilon}_0}{(n+2)\sigma_0^n}\right)^{\frac{n+1}{n}} h^{n+2}|\frac{\partial P}{\partial x}|^n\text{sign}(\frac{\partial P}{\partial z}) \tag{71}$$

Combine the equation (70) and (71):

$$\left(\frac{2\sqrt{3^{n+1}}\dot{\varepsilon}_0}{(n+2)\sigma_0^n}\right)^{\frac{n+1}{n}} h^{n+2}\left|\frac{\partial P}{\partial x}\right|^n \text{sign}\left(\frac{\partial P}{\partial z}\right) = -2\dot{\mathrm{h}}\mathrm{x} \tag{72}$$

Consider the boundary condition of P=0 at the location x=±a, and:

$$\mathrm{F} = 2\mathrm{l}\int_{-a}^{a} P\ dx \tag{73}$$

where *F* is the force load on the surface; then integrating the equation (72), the viscoelastic material force-displacement relationship is obtained:

$$\frac{dh}{dt} = -h\dot{\varepsilon}_0\left(\frac{1}{n+2}\right)\left(\frac{2n+1}{n}\right)^n\left(\frac{\sqrt{3}}{A}\right)^{n+1}(\frac{F/(4al)}{\sigma_0})^n \tag{74}$$

where *a* and *l* are the relevant width and length of the layer; here, only *h* is a variable, other parameters are all constant. Equation (74) can be rewritten as:

$$\dot{\varepsilon}_n^v = \dot{\varepsilon}_0[\left(\frac{1}{n+2}\right)\left(\frac{2n+1}{n}\right)^n\left(\frac{\sqrt{3}}{A}\right)^{n+1}](\frac{\sigma_n}{\sigma_0})^n \tag{75}$$

Eq. (75) shows the pure viscosity of a material. When elasticity is taken into consideration. The constitutive model is composed of a spring in series with the nonlinear dashpot denoted as:

$$\dot{\varepsilon}_n^0 = \dot{\varepsilon}_n^e + \dot{\varepsilon}_n^v = \frac{\dot{\sigma}_n}{E_n} + \dot{\varepsilon}_0[\left(\frac{1}{n+2}\right)\left(\frac{2n+1}{n}\right)^n\left(\frac{\sqrt{3}}{A}\right)^{n+1}](\frac{\sigma_n}{\sigma_0})^n \tag{76}$$

where $\dot{\varepsilon}_n^0$ is the total strain which includes elastic and viscous parts. This is the microscopic constitutive model for a thin film viscoelastic material.

7.2 Model development and verification

On the basis of Eq. (76), a constitutive contact model is deduced to apply in the DEM:

$$\dot{u} = \frac{\dot{f}}{E_n} + \dot{\varepsilon}_0[\left(\frac{1}{n+2}\right)\left(\frac{2n+1}{n}\right)^n\left(\frac{\sqrt{3}}{A}\right)^{n+1}](\frac{f}{\sigma_0})^n \tag{77}$$

where u is the contact overlap and f is the contact force. Then applying a central difference approximation of a finite different scheme, we can obtain the final equation applied in the DEM contact model:

$$\frac{u^{t+1}-u^t}{\Delta t} = \frac{f^{t+1}-f^t}{\Delta t \times E_n} + \dot{\varepsilon}_0[\left(\frac{1}{n+2}\right)\left(\frac{2n+1}{n}\right)^n\left(\frac{\sqrt{3}}{A}\right)^{n+1}](\frac{f^{t+1}+f^t}{2\sigma_0})^n \tag{78}$$

where u^{t+1} is the current contact overlap which has been updated by Newton’s Second Law automatically; u^t and f^t are obtained from the previous time step; and $\mathrm{f}^{\mathrm{t+1}}$ is the only unknown variable – a contact force, needed to be calculated through contact model in the current time step. Therefore, Eq. (78) is a solvable equation that can be applied in DEM directly.

This power law user-defined contact model is written into PFC 3D with the C++ language. After the key equation -- Eq.(78)-- is written into the interface between C++ and FISH, which is the official coding language for PFC 3D, a DLL file is generated by compiling the C++ project, and this DLL file allows the new contact model to be loaded in PFC 3D directly. When the user contact model is running, the updated contact force is obtained through Eq.(78) using the velocity, displacement and force in the previous time step and the Newton method is applied to solve the high order equations. The detailed algorithm in the interface is shown in Figure

7.2, and the key part of C++ code is attached in Appendix A.

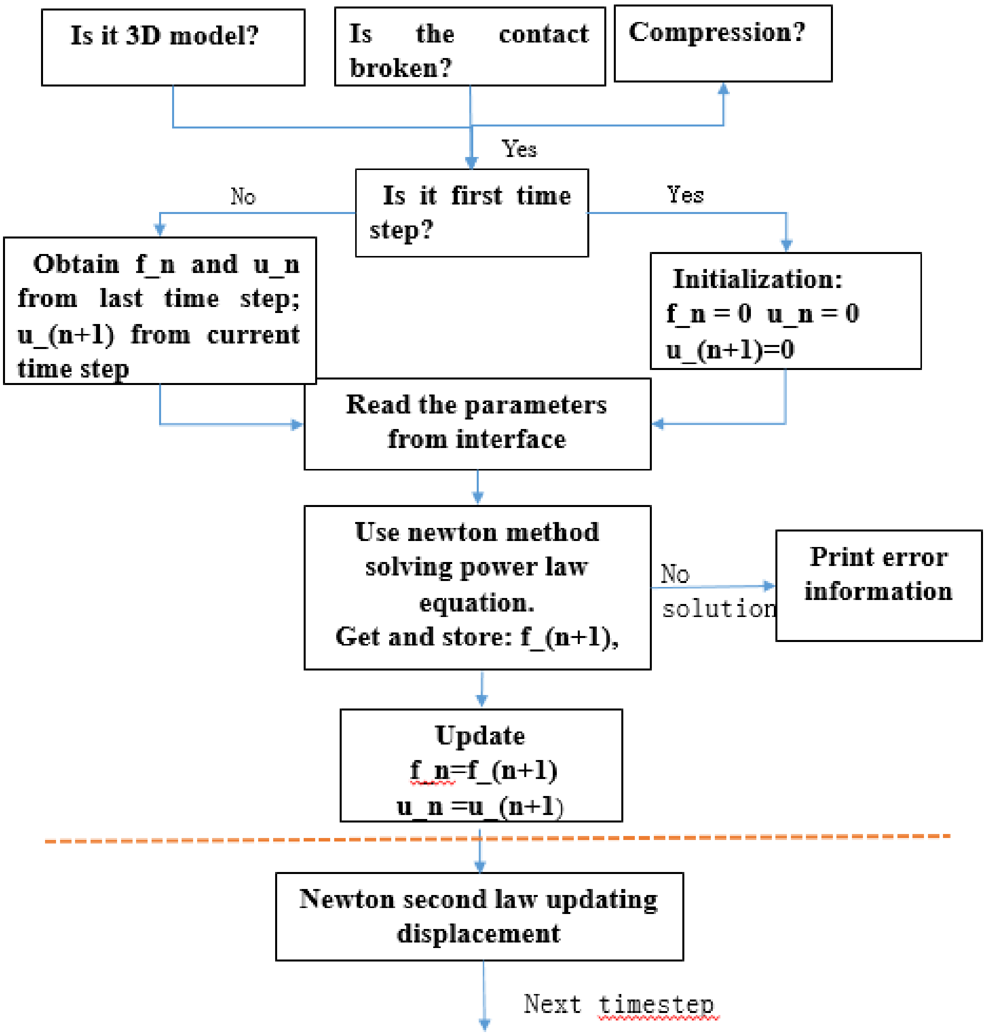

FIGURE 7.2 Chart flow for power law contact model

To verify this contact model, a model of two fixed balls with constant overlap is developed in PFC 3D, as Figure 2.2(a) shows. In this case, since overlap *u* is a constant, Eq. (77) can be simplified as:

$$\dot{f} = -kf^n \tag{79}$$

where $k = E_n \frac{\dot{\varepsilon}_0}{\sigma_0^n} [\left(\frac{1}{n+2}\right)\left(\frac{2n+1}{n}\right)^n \left(\frac{\sqrt{3}}{A}\right)^{n+1}]$

Take n=2 as test case, the theoretical solution for Eq. (79) would be:

$$f(t) = \frac{1}{kt+({}^{1}/_{F_0})} \tag{80}$$

where F_0 is the initial contact force when t=0.

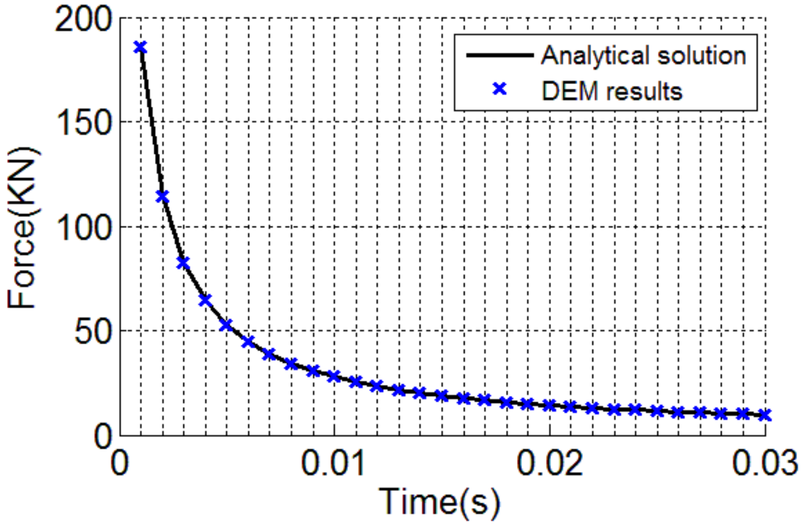

FIGURE 7.3 Comparison between computed result and analytical result.

The black line in Figure 7.3 shows the analytical results calculated by Eq. (80), and the blue dot line is the contact force obtained from the two fixed ball model in PFC 3D. Analytical results and computed DEM results from the power law contact model match well, verifying the power law's solution is successfully integrated into the DEM contact model. Both lines demonstrate that the force vanishes to zero with time, which is consistent with a viscosity material under constant loading.

7.3 Experiment validation

In order to develop the experimental situation consistent with power law theory—a thin film layer between two rigid planes, a sample is prepared as a thin film asphalt sandwiched between two cubic aggregates. Unakite aggregates are used in this experiment. In comparison with the stiffness of asphalt, the stiffness of Unakite aggregates is very large and can be considered as rigid. PG70-34 binder is used in the tests. After the binder was heated to 300 ℉, a slight amount of softened binder was positioned over one aggregate, and another aggregate is used to cover the other surface of asphalt binder immediately. When the temperature goes down, asphalt shrinkage is inevitable. To neutralize the tension caused by shrinkage during the asphalt cooling down, the sample is pressed gently. This pressure assists in the formation of a thinner and more evenly distributed asphalt layer.

Because of the high energy of X-ray, the temperature within the machine will slightly increase. In this case, it is very important to finish the tests as soon as possible to keep testing times the same. Testing parameters are set through software controlling the X-ray system. With a constant speed of 0.7 μm, the force-displacement relationship is recorded during uniaxial compression process.

To verify the correctness and accuracy of power law contact model, two sets of tests are performed. The parameters are provided in Table 1.

TABLE 1 Sample Information

	Thickness of asphalt lay (μm)	**Width of asphalt lay (mm)**	**Aspect ratio of asphalt layer**	**Aggregate Material**	**Plane size of stone (mm)**
Experiment 1	156	3.92	25.13	Unakite	4.29*4.29
Experiment 2	156	3.5	22.44	Unakite	4.29*4.29

After the force-displacement data is obtained from SKYSCAN, a curve fitting method is applied to obtain the parameters of the contact model in Eq. (78). To simplify the process, three reorganized parameters are estimated:

$$a_1 = E_n \tag{81}$$

$$a_2 = \frac{\dot{\varepsilon}_0}{\sigma_0^n} \tag{82}$$

$$a_3 = [\left(\frac{1}{n+2}\right)\left(\frac{2n+1}{n}\right)^n\left(\frac{\sqrt{3}}{A}\right)^{n+1}] \tag{83}$$

The curve fitting solution employs an ordinary differential equation (ODE) solver and a fmincon function in MATLAB to find the minimal difference between experimental results and computational ODE results. To acquire accurate fitted curve and estimated parameters, the initial values of the parameters are very important. Without a reasonable initial value, the fmincon function has a high possibility to find a local minimum, whereas only the global minimum is the desired answer. Supposing n=2, this process will only obtain material-related parameters a_1, a_2, because a_3 can be directly calculated when the geometry information is known.

To evaluate the accuracy of power law model, material parameters a_1, a_2 estimated from test 2 and geometric parameter a_3 from test 1 are applied in DEM model, which is used for comparison with experimental data 1. Vice versa, DEM data by a_1, a_2 from test 1 and a_3 from test 2 are compared with experimental data 2.

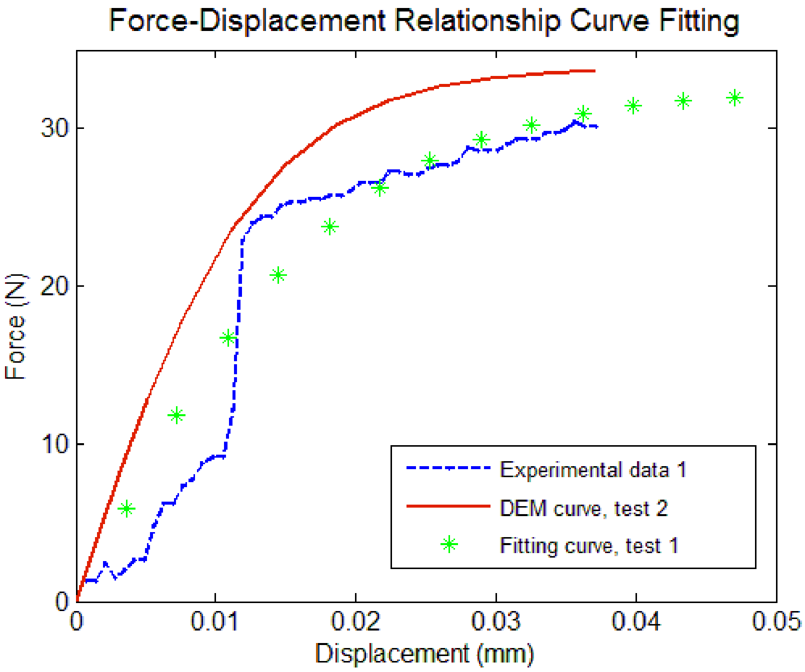

FIGURE 7.4 Experimental, numerical, DEM results for experiment 1

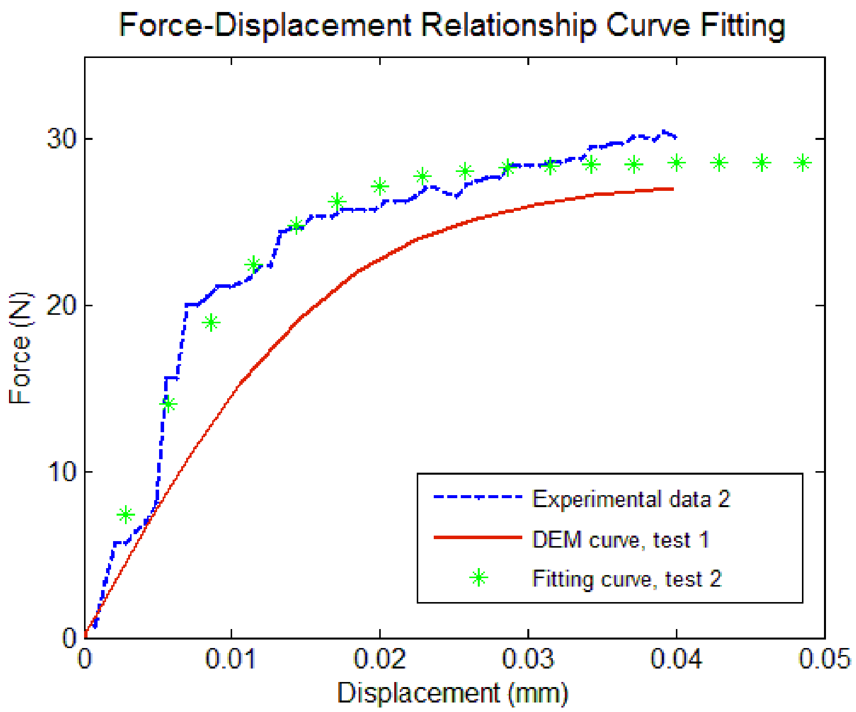

FIGURE 7.5 Experimental, numerical, DEM results for experiment 2

In Figure 7.4 and Figure 7.5, the blue dashed line presents the experiment results, the green dots represent the fitted curve where the material parameters are obtained from the same test and the red line demonstrates the numerical results with material parameters from another experiment. For the experimental data, the general trend of force-displacement obeys the viscoelastic law, which is near elastic at the beginning, and gradually plateaus. In terms of how well the power law model fits with the experimental results, an average error is calculated -- average absolute value of force difference between experimental data and power law numerical data:

$$F_{err} = \frac{1}{n}\sum_{i=1}^{n} |F_{simulation} - F_{experiment}| \tag{84}$$

and relative error percentage is defined as force error divided by maximum experimental force after its increasing rate stabilized:

$$\mathrm{P} = F_{err}/F_{average} \tag{85}$$

The detailed results are shown in Table 2. The columns in the table represent the experiment results used for comparison, and the rows describe the data sets used for material parameters estimation, which are applied to numerical results. As the table shows, errors are relatively small when the same test data is used for parameter estimating and error testing – 7.8% for test 1 and 3.36% for test 2. The maximum numerical force error is 5.3 N, after divided by the stable force in the experiment — 30.1 N, the relative error does not exceed 17%.

There are several reasons that cause the error. First, the two planes of aggregates sandwiched asphalt binder are not strictly parallel to each other. Second, the friction of aggregate surface is not large enough to ensure the theoretical boundary condition. Third, the lateral deformation in both directions along the plane is not even.

TABLE 2 Error information between experiment results and DEM results

Parameter From / **Test Data**	**Force Error (N)**		**Error Percentage**	
	Test 1	**Test 2**	**Test 1**	**Test 2**
Test 1	2.357	5.314	7.83%	17.65%
Test 2	3.551	1.0117	11.80%	3.36%

Chapter 8 CALCULATION TIME FOR EACH CONTACT MODEL

Computational cost is a very important factor for simulations, due to the limitation of computing power. If a contact model is too complicated, then it is not practical in the application for a large model with a long simulation time. Therefore, a test on comparing computational time costs for each contact model is derived to evaluate the model complexity.

In this simulation test, 200 particles are generated. They are arranges in two planes, and there are 100 contacts in total. Compression, tension and tangential force are loaded in this model in three different tests separately, as Figure 8.1 shows. The time for 50000 calculation cycles are recorded for each contact model, and results are shown in Table 2.

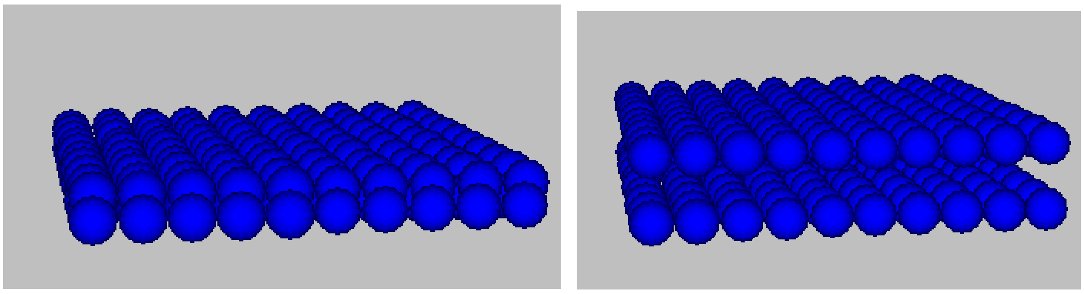

(a) In compression **(b) In tension**

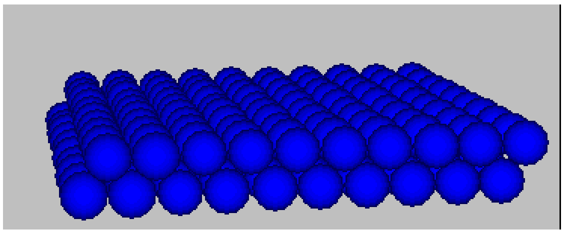

(c) In tangential direction

FIGURE 8.1 Model for calculation time tests

	compression	tension	shear
Linear	15	X	13
Hertz	11	X	15
Simple viscoelastic	81	63	78
Burger	60	78	61
Simple ductile	51	53	56
Displacement softening	325	330	340

TABLE 3 Computation time for different contact models (seconds)

From Table 3, it shows that a linear elastic model and a Hertz-Mindlin model have a fairly similar calculation complexity. In the case of viscoelastic, both Burger model and simple viscoelastic model cost time are around 60-80 seconds. But in the case of ductility, the displacement softening model costs 6 times more than the simple ductile contact model in loading of compression, tension and shear force. Therefore, we can conclude that, the elastic model is the simplest model, and costs the least time. When simulating viscoelastic behavior, the Burger model is a better choice than a simple elastic model, since it is able to provide relatively accurate results while costing the same amount of computational time. In the ductile simulation, though a softening model more accurately presents ductile behaviors, additional time costs would be a weakness for large computation tasks.

Chapter 9 CONCLUSIONS

Six existing typical contact models that can be applied to pavement simulations are reviewed in detail: linear elastic, hertz elastic, simple viscoelastic, Burger model, simple ductile, and displacement softening model. Their mechanical behavior curves are presented for loading in compression, tension and tangential directions. The complexity of the models is verified by comparing their calculation time cost, which serves as a good reference for future researchers to choose contact models according to the size of their simulation.

- Elastic contact mode: linear elastic model can simulate elastic continuum material with reasonable accuracy, and Hertz-Mindlin is good for the simulation focused on sphere shape contact.
- Viscosity: simple ductile contact model only shows viscosity in the shear direction. Compared to the simple viscoelastic model, the Burger model is a better choice when simulations focus on compression, and due to the combination of the Maxwell model and Kelvin model, the Burger model has more flexibility.
- Ductility: both the simple ductile model and the displacement softening model are able to simulate plasticity, while the displacement softening model takes plastic deformation in both directions and material yielding in the shear direction into consideration. Though the displacement softening model is with higher accuracy than ductile model, it costs almost 5 times more calculation time than the simple ductile model.

As a new alternative contact model for asphalt binder simulation, the power law model shows a good potential to solve thin film asphalt problems. With the corresponding power law

DLL file generated by C++ code, the new contact model is able to be loaded directly into PFC 3D to apply to more complex problems. However, some interesting problems are also raised during this research. How does film thickness influence the accuracy of power law model? How does aggregate stiffness and friction affect experimental results? What is the force (stress) range that the power law model is good for? Can we use more parameters to calibrate power law model and improve model accuracy? This thesis provides a foundation for further exploration and future work.

REFERENCES

Abbas, A., Masad, E., Papagiannakis, T., and Harman, T. (2007). "Micromechanical modeling of the viscoelastic behavior of asphalt mixtures using the discrete-element method." *International Journal of Geomechanics*, 7(2), 131-139.

Adams, G., and Nosonovsky, M. (2000). "Contact modeling—forces." *Tribology International*, 33(5), 431-442.

Aoki, K. M., and Akiyama, T. (1995). "Simulation studies of pressure and density wave propagations in vertically vibrated beds of granules." *Physical Review E*, 52(3), 3288.

Baumgaertel, M., and Winter, H. (1989). "Determination of discrete relaxation and retardation time spectra from dynamic mechanical data." *Rheologica Acta*, 28(6), 511-519.

Cheung, C., and Cebon, D. (1997). "Thin film deformation behavior of power-law creeping materials." *Journal of engineering mechanics*, 123(11), 1138-1152.

Chow, C., and Wang, J. (1987). "An anisotropic theory of continuum damage mechanics for ductile fracture." *Engineering Fracture Mechanics*, 27(5), 547-558.

Collop, A. C., McDowell, G. R., and Lee, Y. (2004). "Use of the distinct element method to model the deformation behavior of an idealized asphalt mixture." *International Journal of Pavement Engineering*, 5(1), 1-7.

Cundall, P. A., and Strack, O. D. (1979). "A discrete numerical model for granular assemblies." *Geotechnique*, 29(1), 47-65.

Di Maio, F., and Di Renzo, A. (2005). "Modelling particle contacts in distinct element simulations: Linear and non-linear approach." *Chemical Engineering Research and Design*, 83(11), 1287-1297.

Di Renzo, A., and Di Maio, F. P. (2004). "Comparison of contact-force models for the simulation of collisions in DEM-based granular flow codes." *Chemical Engineering Science*, 59(3), 525-541.

Di Renzo, A., and Di Maio, F. P. (2005). "An improved integral non-linear model for the contact of particles in distinct element simulations." *Chemical engineering science*, 60(5), 1303-1312.

Hamaker, H. (1937). "The London—van der Waals attraction between spherical particles." *physica*, 4(10), 1058-1072.

Hertz, H. (1881). "On the contact of elastic solids." *J. reine angew. Math*, 92(156-171), 110.

Kruggel-Emden, H., Simsek, E., Rickelt, S., Wirtz, S., and Scherer, V. (2007). "Review and extension of normal force models for the discrete element method." *Powder Technology*, 171(3), 157-173.

Kruggel-Emden, H., Wirtz, S., and Scherer, V. (2008). "A study on tangential force laws applicable to the discrete element method (DEM) for materials with viscoelastic or plastic behavior." *Chemical Engineering Science*, 63(6), 1523-1541.

Krupp, H. (1967). *Particle adhesion, theory and experiment*, Advan. Colloid Interface Sci. 1 (1967), 111-239.

Kuwabara, G., and Kono, K. (1987). "Restitution coefficient in a collision between two spheres." *Japanese journal of applied physics*, 26(8R), 1230.

Itasca. *Particle flow code 3D manual: Background and theory*. Minneapolis, Minnesota, 2008

Langston, P., Tüzün, U., and Heyes, D. (1994). "Continuous potential discrete particle simulations of stress and velocity fields in hoppers: transition from fluid to granular flow." *Chemical Engineering Science*, 49(8), 1259-1275.

Lee, J., and Herrmann, H. J. (1993). "Angle of repose and angle of marginal stability: molecular dynamics of granular particles." *Journal of Physics A: Mathematical and General*, 26(2), 373.

Lemaitre, J. (1984). "How to use damage mechanics." *Nuclear Engineering and Design*, 80(2), 233-245.

Limtrakul, S., Boonsrirat, A., and Vatanatham, T. (2004). "DEM modeling and simulation of a catalytic gas–solid fluidized bed reactor: a spouted bed as a case study." *Chemical Engineering Science*, 59(22), 5225-5231.

Maw, N., Barber, J., and Fawcett, J. (1976). "The oblique impact of elastic spheres." *Wear*, 38(1), 101-114.

Mindlin, R. D., and Deresiewica, H. (2013). "Elastic spheres in contact under varying oblique forces." *Journal of applied mechanics*, 20.

Papagiannakis, A., Abbas, A., and Masad, E. (2002). "Micromechanical analysis of viscoelastic properties of asphalt concretes." *Transportation Research Record: Journal of the Transportation Research Board*, 1789(1), 113-120.

Sadd, M. H., Tai, Q., and Shukla, A. (1993). "Contact law effects on wave propagation in particulate materials using distinct element modeling." *International Journal of Non-Linear Mechanics*, 28(2), 251-265.

Shäfer, J., Dippel, S., and Wolf, D. (1996). "Force schemes in simulations of granular materials." *Journal de physique I*, 6(1), 5-20.

Shalaby, A. (2002). "Modelling short-term aging of asphalt binders using the rolling thin film oven test." *Canadian Journal of Civil Engineering*, 29(1), 135-144.

Thornton, C. (1997). "Coefficient of restitution for collinear collisions of elastic-perfectly plastic spheres." *Journal of Applied Mechanics*, 64(2), 383-386.

Thornton, C., and Ning, Z. (1998). "A theoretical model for the stick/bounce behaviour of adhesive, elastic-plastic spheres." *Powder technology*, 99(2), 154-162.

Thornton, C., and Yin, K. (1991). "Impact of elastic spheres with and without adhesion." *Powder technology*, 65(1), 153-166.

Tomas, J. (2003). "Mechanics of nanoparticle adhesion–a continuum approach." *Particles on surfaces*, 8, 183-229.

Tsuji, Y., Kawaguchi, T., and Tanaka, T. (1993). "Discrete particle simulation of two-dimensional fluidized bed." *Powder technology*, 77(1), 79-87.

Tsuji, Y., Tanaka, T., and Ishida, T. (1992). "Lagrangian numerical simulation of plug flow of cohesionless particles in a horizontal pipe." *Powder technology*, 71(3), 239-250.

Vu-Quoc, L., and Zhang, X. (1999). "An elastoplastic contact force–displacement model in the normal direction: displacement–driven version." *Proceedings of the Royal Society of London. Series A: Mathematical, Physical and Engineering Sciences*, 455(1991), 4013-4044.

Vu-Quoc, L., Zhang, X., and Lesburg, L. (2001). "Normal and tangential force–displacement relations for frictional elasto-plastic contact of spheres." *International journal of solids and structures*, 38(36), 6455-6489.

Walton, O. R. (1993). "Numerical simulation of inclined chute flows of monodisperse, inelastic, frictional spheres." *Mechanics of Materials*, 16(1), 239-247.

Walton, O. R., and Braun, R. L. (1986). "Viscosity, granular‐temperature, and stress calculations for shearing assemblies of inelastic, frictional disks." Journal of Rheology (1978-present), 30(5), 949-980.

Wang, Dong (2007), “Binder film thickness effect on aggregate contact behaviors”, Virginia Tech, Blacksburg, VA. Used under fair use, 2014.

Zhang, D., and Whiten, W. (1996). "The calculation of contact forces between particles using spring and damping models." *Powder technology*, 88(1), 59-64.

Zhu, H., Zhou, Z., Yang, R., and Yu, A. (2007). "Discrete particle simulation of particulate systems: theoretical developments." *Chemical Engineering Science*, 62(13), 3378-3396.

Zhu, H., Zhou, Z., Yang, R., and Yu, A. (2008). "Discrete particle simulation of particulate systems: a review of major applications and findings." *Chemical Engineering Science*, 63(23), 5728-5770.

Appendix A – The key part C++ code for power law contact model

```
void USERCM1::FDlaw(FdBlock& fb, char cDim) {
         double con1;
         double con2;
         double u_n1=fb.u_n;
         double con3;
         double sq3;
         sq3=sqrt(3.0);

if (CDim=3) { // ... 3D section ...
       if(fb.tdel!=tdel)
       {
           tdel=fb.tdel;
       }
       if(mark==0)
       {
          f_n0=kn*fb.u_n;
          u_n0=fb.u_n;
       }
         if (fb.u_n > 0.0||fb.bflag) {
              mark++;//to see whether t=0 or not.
              con1=strain_rate_0*(1/(nn+2)*pow((2*nn+1)/nn,nn)*pow(sq3/A,nn+1));
              con2=con1*tdel*kn/pow(2*stress0,nn);//constant for nn order
              con3=-2*f_n0-kn*(u_n1-u_n0);//constant for 0 order
              fb.n_force=newton(con2,nn,1,1,con3)-f_n0;//x is f(t+1)+f(t)
              if (fb.n_force==-1)fb.n_force=f_n0;
              f_n0=fb.n_force;
              u_n0=u_n1;
              }
                   else {
                fb.knest = 0.0;
                fb.ksest = 0.0;
               fb.skip   = true;
              }
     }

}

double ff(double xx,double conn1, double nn1,double conn2,double n2,double conn3)
{
     return conn1*pow(xx,nn1)+conn2*pow(xx,n2)+conn3;
}
```

```
double fpri(double xx,double conn1, double nn1,double conn2,double n2,double conn3)
{
    return conn1*nn1*pow(xx,nn1-1)+conn2*pow(xx,n2-1);
}
double newton(double conn1, double nn1,double conn2,double n2,double conn3)
{
    double y1=-1;
    double x1,x2,yp;
    double MAX_run=5000;
    int mark_newton=0;
    y1=ff(0,conn1,nn1,conn2,n2,conn3);
   yp=fpri(0,conn1,nn1,conn2,n2,conn3);
   x1=abs(y1/yp);
    y1=ff(x1,conn1,nn1,conn2,n2,conn3);//y1 should be larger or equal to zero
    while(abs(y1)>=0.001 && mark_newton<=MAX_run)
    {
        mark_newton++;
        yp=fpri(x1,conn1,nn1,conn2,n2,conn3);
        if(yp==0)
        {
            y1+=1000;
            continue;
        }
        if(y1>=0)  //using this jusgement, then make sure a point f(y)>0 would be found
        x1=x1-y1/yp;
        else
        x1=x1+abs(y1/yp)+10000;  //+10000 is to void the case yp is nearly  y1.
        y1=ff(x1,conn1,nn1,conn2,n2,conn3);
    }
    if (mark_newton<=MAX_run)
        return x1;
    else
        return -1;
}
```